Oceanologia (2019) 61, 484—504

Available online at www.sciencedirect.com

ScienceDirect

journal homepage: www.journals.elsevier.com/oceanologia/

ORIGINAL RESEARCH ARTICLE

Recent sea surface temperature trends and future scenarios for the Red Sea

Mohamed Shaltout *

Faculty of Science, Department of Oceanography, University of Alexandria, Alexandria, Egypt

Received 10 September 2018; accepted 7 May 2019
Available online 24 May 2019

KEYWORDS
Red Sea;
Sea surface temperature;
Chlorophyll-*a*;
Heat exchange;
Climate models;
Ensemble forecast

Summary The current paper analyses the recent trends of Red Sea surface temperature (SST) using 0.25° daily gridded Optimum Interpolation Sea Surface Temperature (OISST) data from 1982 to 2016. The results of 3 different GFDL (Geophysical Fluid Dynamics Laboratory) model simulations are used to project the sea surface temperature (hereafter called Tos) under the four representative concentration pathway scenarios through 2100.

The current research indicates that the spatially annual mean (from 1982 to 2016) Red Sea surface temperature is 27.88 ± 2.14°C, with a significant warming trend of 0.029°C yr^{-1}. The annual SST variability during the spring/autumn seasons is two times higher than during the winter/summer seasons. The Red Sea surface temperature is correlated with 13 different studied parameters, the most dominant of which are mean sea level pressure, air temperature at 2 m above sea level, cross-coast wind stress, sensible heat flux, and Indian Summer Monsoon Index.

For the Red Sea, the GFDL-CM3 simulation was found to produce the most accurate current SST among the studied simulations and was then used to project future scenarios. Analysis of GFDL-CM3 results showed that Tos in the Red Sea will experience significant warming trends with an uncertainty ranging from 0.6°C $century^{-1}$ to 3.2°C $century^{-1}$ according to the scenario used and the seasonal variation.

* Corresponding author at: Laboratory Faculty of Science, Department of Oceanography, University of Alexandria, Alexandria 21151, Egypt. Tel.: +20 1005255393; fax: +203 3911794.
E-mail address: mohamed.shaltot@alexu.edu.eg.

Peer review under the responsibility of Institute of Oceanology of the Polish Academy of Sciences.

ELSEVIER | Production and hosting by Elsevier

https://doi.org/10.1016/j.oceano.2019.05.002

1. Introduction

The Red Sea and its surrounding sea region (Gulf of Aden) extending from 32°E to 51°E and from 10°N to 30°N (hereafter "Red+"; Fig. 1) can be divided into several subbasins, for example, the Gulf of Aden subbasin (hereafter "GOA subbasin") south of Bab el-Mandeb Strait, Southern Red Sea (SRed), Central Red Sea (CRed) and Northern Red Sea (NRed). Red+, which is considered an arid climate region with negligible precipitation and runoff (Al-Horani et al., 2006), provides a significant resource for tourism, fishing, coral reefs, and oil and gas extraction. Moreover, the Red Sea supports a high volume of shipping activity, which links European harbors to China and eastern Asia. The vulnerability of Red+ to SST warming trends during the current century is highly expected (Hoegh-Guldberg et al., 2014), which may lead to a potentially harmful impact on marine entities and ecosystems (e.g., the decline in the average coral colony size). The IPCC (2014) shows that the global SST will experience warming trends during the current century. The warming trends are expected to continue even if greenhouse gas emissions remain constant or decrease (Collins et al., 2013).

During the 1950–2007 period, the Red Sea SST reached its highest value during August and reached its lowest value during February (Hoegh-Guldberg et al., 2014). The Red Sea's seasonal summer to winter SST difference is approximately 6°C (Berman et al., 2003). In a study of the Red Sea SST during the period 1985–2007, Raitsos et al. (2011) found that the coldest year was 1992 and that the annual mean SST was 27.4°C from 1985 to 1993 and 28.1°C from 1994 to 2007.

Raitsos et al. (2011) also confirmed that there was intense warming of the Red Sea surface temperature in the mid-90s. Hoegh-Guldberg et al. (2014) found no significant trend in the Red Sea surface temperature from 1950 to 2007. However, there was a significant warming from 1982 to 2006, indicating

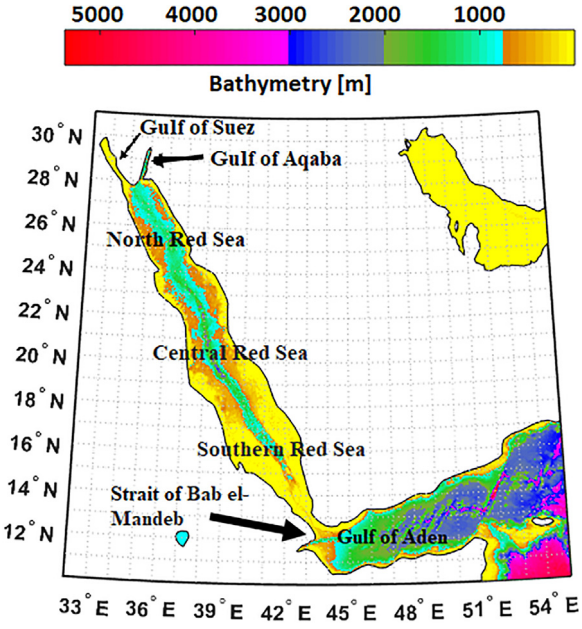

Figure 1 Bathymetric chart of the Red Sea (data acquired from a global 30 arc-second interval grid (GEBCO: https://www.gebco.net/data_and_products/gridded_bathymetry_data/)).

that the absence of a significant trend in the Red Sea surface temperature over the long period of 1950 to 2007 may be caused by the large-scale variability prior to 1982, which may be due to the influence of the Atlantic Multidecadal Oscillation (AMO) and North Atlantic Oscillation (NAO). In addition, the authors noted that the Red Sea SST exhibits a significant trend of 0.5 and 0.3°C decade^{-1} for the warmest and coolest months, respectively. The Red Sea surface temperature warming trends are spatially distributed, most clearly in the central Red Sea for the period 1950–1997 [0.31°C decade^{-1}] (Cantin et al., 2010). Recently, Chaidez et al. (2017) showed that the maximum Red Sea temperature experienced a warming trend of 0.017°C yr^{-1} for the 1982–2015 period. They found that the Gulfs of Suez and Aqaba exhibit lower temperatures than the open Red Sea. Moreover, the maximum Red Sea temperature occurred during July in the northern Red Sea and from late July to mid-August in the southern Red Sea. Karnauskas and Jones (2018) showed that the interannual variability of the Red Sea SST occurs in both summer and winter, most markedly in NRed during winter.

Heat waves were observed more frequently in the northern half of the Red Sea over the period 1982–2015 (Chaidez et al., 2017). Thomas et al. (2012) and Sawall et al. (2014) showed that the warming process in the Red Sea may lead to thermal collapse (thermal collapse occurs when the temperature exceeds the thermal capacity of organisms).

The Red Sea SST is significantly affected by the Indian monsoon (Raitsos et al., 2011). The Atlantic Multidecadal Oscillation Index (AMOI) and North Atlantic Oscillation Index (NAOI) have an effect on the Red Sea SST long-term variability (Hoegh-Guldberg et al., 2014). The SST is mainly affected by the air temperature at 2 m above sea level (T_{2m}), mean sea level pressure (SLP), total cloud cover (TCC), wind stress components at 10 m above sea level (i.e., cross-coast surface wind stress (τ_{ac}) and along-coast surface wind stress (τ_{al})) and air-sea heat fluxes (Shaltout and Omstedt, 2014; Skliris et al., 2012).

In general, the exchange through Bab el-Mandeb Strait has a significant effect on SST distribution, especially in SRed. The water exchange through Bab el-Mandeb Strait is described as a two-layer flow during cold months; dense intermediate Red Sea water flows out into the Gulf of Aden and the warmer, fresher surface water from the Gulf of Aden flows into the Red Sea. In the summer season, this exchange represents a three-layer structure; surface and intermediate Red Sea water flow out to the Gulf of Aden; however, a third layer, with a density between that of the surface layer and that of the intermediate Red Sea water, flows into the Red Sea (Smeed, 1997). The summer exchange in the strait is remotely induced by the monsoonal wind over the Indian Ocean (Aiki et al., 2006). During the winter monsoon, the predominant winds over the strait blow towards the Red Sea enhancing the surface layer inflow and bottom layer outflow, whereas, during the summer monsoon, the wind blows toward the Indian Ocean suppressing the surface layer inflow (Aiki et al., 2006).

Clearly, significant warming can potentially lead to ecological collapse (Richardson and Schoeman, 2004). According to Cantin et al. (2010) and Roik et al. (2016), the decrease of coral growth in CRed is a result of warming conditions. In addition, the NRed SST has a significant negative correlation with chlorophyll-*a* (chl-a) concentration (Eladawy et al., 2017). Recently, Osman et al. (2018) showed that the maximum annual water temperatures are close to coral thermal

limits in CRed, however, over NRed corals live well as their thermal limits are not close to maximum annual water temperature. Corals in the northern Red Sea have a much higher heat tolerance than their prevailing temperature regime would suggest. In contrast, corals from the central Red Sea are close to their thermal limits.

Hoegh-Guldberg et al. (2014) have discussed the projected changes of the Red Sea SST up to the end of the current century using AOGCM model simulations from the Coupled Model Intercomparison Project Phase 5 (CMIP5, http://cmip-pcmdi.llnl.gov/cmip5/) under four representative concentration pathway scenarios (i.e., RCP2.6, RCP4.5, RCP6.0, and RCP8.5). They have predicted that the Red Sea SST may experience significant warming ranging from 0.35°C (RCP2.6) to 0.77°C (RCP8.5) over the period from 2010–2039, whereas from 2010–2099 the warming ranges from 0.88°C (RCP2.6) to 3.45°C (RCP8.5).

Although many other works have been published recently about the Red+ SST, studying its maximum values and heat waves characteristics (Chaidez et al., 2017) or studying its interannual variability (Karnauskas and Jones, 2018), the comparison between the 4 Red+ subbasins together with projection of the future Red+ SST scenarios have not received enough attention. Moreover, studying the effect of heat waves on the chl-a concentration for each Red+ SST cluster is quite new. This information is needed to extend our knowledge about the seasonal/spatial variability of the Red+ SST from 1982 through 2100. This information supports the decision makers in reducing the impacts of expected warming trends in Red+, especially on chl-a concentrations.

The present research uses a 35-year (1982–2016) high-resolution SST database: (1) to examine temporal and spatial SST variability in Red+; (2) to analyze the relationship between Red+ SST and various atmospheric parameters, such as T_{2m}, SLP, TCC, τ_{ac}, τ_{al}, air-sea heat fluxes, AMOI, NAOI and Indian Summer Monsoon Index (ISMI); (3) to examine SST characteristics in the different Red+ subbasins (Red+ is treated as 4 sub-basins); (4) to study the effect of heat wave events on chl-a concentrations; and (5) to examine the projected Red+ SST through the year 2100 using available GFDL future simulations. Data and methods used are presented in Section 2, the results and the discussion are in Section 3, and the conclusions are in Section 4.

2. Data and methods

2.1. Data used

This paper analyses the present Red+ SST characteristics and future warming uncertainties based on various available data sources, as follows.

i. Gridded daily 0.25° NOAA Optimum Interpolation Sea Surface Temperature data (OISST; version 2), from 1982 to 2016, were used to study recent SST characteristics. OISST (version 2) merges satellite ocean skin temperatures and in situ platforms (ships and buoys) on a regular global grid (Reynolds et al., 2007; Reynolds, 2009). The in situ platform measurements were acquired from ICOADS (International Comprehensive Ocean-Atmosphere Data Set) (Worley et al., 2005). The methodology includes applying the Optimum Interpolation (OI) statistical method to fill the gaps. Moreover, a bias adjustment step of satellite data to in situ data is performed prior to interpolation. The daily OISST is a combination of data collected over the entire day, so this method does not capture diurnal variability and does not represent a particular time of day (Banzon et al., 2018). These data are freely available as gridded netCDF Data via FTP (ftp://eclipse.ncdc.noaa.gov/pub/OI-daily-v2/NetCDF/). The OISST is relevant to study local oceanic features (Nykjaer, 2009). The OISST database is described as a scientific tool to study SST variability in the Red Sea, especially due to the high density of in situ measurements in the ICOADS data bank of the Red Sea (Karnauskas and Jones, 2018).

ii. In situ SST data were downloaded from various databases:
- WOD2013 – World Ocean Database 2013 (Boyer et al., 2013, http://www.nodc.noaa.gov/). The WOD2013 data are mostly collected from multiple datasets: Ocean Station Data (**OSD**), Conductivity-Temperature-Depth (**CTD**) data, **MBT** (Mechanical Bathythermograph) data, expendable bathythermograph (**XBT**), and drifting buoy (**DRB**) data.
- GOSUD – Global Ocean Surface Underway data (GOSUD, 2016, https://www.seanoe.org/data/00363/47403/). The GOSUD data are mostly collected using thermosalinographs (TSG) installed on research vessels, on commercial ships and, in some cases, on sailing exploration ships. GOSUD manages delayed-mode together with near-real-time data. The methods contain a quality control process.

iii. Simulated surface circulation data were extracted from the HYbrid Coordinate Ocean Model (HYCOM) daily output with 1/12° horizontal grid resolution and 32 vertical layers. These data can be freely accessed from ftp://ftp.hycom.org/datasets/GLBa0.08/ for the 2007–2016 period. The HYCOM is a primitive equation ocean general circulation model that evolved from the MICOM (Miami Isopycnic-Coordinate Ocean Model) as described in Halliwell (2004). HYCOM is relevant to study the Red Sea surface circulation (Eladawy et al., 2017).

iv. Atlantic Multidecadal Oscillation Index (AMOI), North Atlantic Oscillation Index (NAOI) and Indian Summer Monsoon Index (ISMI) data were used to study the link between climate indices and Red+ SST.
- Monthly AMOI captured by the NOAA Earth System Research Laboratory (https://www.esrl.noaa.gov/psd/data/correlation/amon.us.data) over the period from 1982 to 2016 were used. The AMOI is characterized by the annual mean area-average of detrended SST anomalies over the North Atlantic from 0°N to 60°N. Detrended SST anomalies are derived by removing the global mean SST time series from each grid point (Trenberth and Shea, 2006).
- Daily NAOI data from 1982 to 2016 were extracted from the KNMI Climate Explorer (https://climexp.knmi.nl). The NAOI is the sea level pressure (SLP) difference between the high latitudes of the North Atlantic and the central latitudes of the North Atlantic, which are from 30°N to 40°N. The negative phase of the NAOI reflects below-normal SLP over the central North Atlantic and above-normal SLP across the

high latitudes of the North Atlantic. The positive phase describes the opposite pattern (Hurrell, 1995).

- Daily ISMI data were extracted from the Asia-Pacific Data-Research Center (http://apdrc.soest.hawaii.edu/projects/monsoon/daily-data.html#mon) from 1982 to 2015. The ISMI lasts only from June until September and contributes to temperature distribution and wind circulation (Sarthia et al., 2012). The ISMI is an 850-hPa zonal wind difference between a southern region (40°–80°E, 5°–15°N) and a northern region (70°–90°E, 20°–30°N) as described in Wang et al. (2001). The strength of an Indian summer monsoon system increases with the increase of ISMI positive values.

v. Gridded daily data, from 1982 to 2016, on several surface meteorological parameters (T_{2m}, SLP, and TCC) and air-sea heat fluxes were extracted from the ERA-Interim full-resolution (0.125° × 0.125°) database (http://apps.ecmwf.int/datasets/data/interim-full-daily/levtype=sfc/). Era-Interim data were originally of a 0.75° × 0.75° grid size and recently were bilinearly interpolated to a 0.125° grid to provide a finer resolution (Owens and Hewson, 2018). This interpolation employs a land-sea mask to decrease undesired smoothing of gradients along coastlines; thus, Era-Interim fine-resolution (0.125°) data were used in the current study to study their relationship to the SST dynamic. Surface metrological parameters are produced with the observation fields; however, air-sea heat fluxes are produced with a forecasting model. The forecasting model uses the Monin–Obukhov formulation (Dee et al., 2011; Zhou and Wang, 2016).

vi. Daily surface wind speed components were extracted from the ERA-Interim full-resolution (0.125° × 0.125°) database from 1982 to 2000. From 2000 to 2016, remotely sensed daily ocean with 0.25° grid resolution wind data were used; the Quick Scatterometer (QUICK SCAT; Ricciardulli et al., 2011) from 2000 to 2007 and Advanced Scatterometer (ASCAT) wind maps (Bentamy and Croize-Fillon, 2012) from 2007 to 2016 were used. QUICK SCAT and ASCAT data were freely accessed via (ftp://ftp.ifremer.fr/ifremer/cersat/products/gridded/MWF/L3/).

vii. Gridded daily data on chlorophyll-*a* (chl-a) concentrations were extracted from the MODIS (Moderate Resolution Imaging Spectroradiometer) sensor database. MODIS, which is a sensor operating on the NASA Aqua satellite, was launched on May 2002 to support scientists to study global change with many standard data products. The current paper uses the Level 3 standard mapped image (SMI, MODIS_L3_Chl-a) to study the variability of chl-a concentration over Red+. MODIS_L3_Chl-a dataset validations and documentations are fully described in Anonymous (2014). These data are freely available with a 4.6 km (at the equator) spatial resolution from 2003 to 2016 via https://oceandata.sci.gsfc.nasa.gov/MODIS-Aqua/Mapped/Daily/4km/chlor_a/. Many authors have used MODIS_L3_Chl-a to study marginal seas including Red+ (Bai et al., 2018; Eladawy et al., 2017). Moreover, MODIS_L3_Chl-a has shown very good agreement with in situ data in the Red Sea (Brewin et al., 2013).

viii. Future SST (hereafter, Tos): Model output from three different GFDL simulations for current century CMIP5 scenarios (i.e., RCP2.6, RCP4.5, RCP6.0, and RCP8.5) were used. RCP stands for "Representative Concentration Pathways," and the following numbers indicate the assumed radiative forcing in 2100. These data were used to project SST uncertainty up to 2100. GFDL simulation is based on coupled atmospheric/oceanic circulation models with respect to land and iceberg dynamics (Delworth et al., 2006; Dunne et al., 2013) to understand future climate behavior.

2.2. Estimated quality of the OISST database used for the study area

A direct comparison of the spatiotemporal Red+ SST variability between the OISST data and in situ SST data were used to test the quality of OISST database over Red+ during the overlapping period (1982–2012). Thus, the correlation coefficients (R) and the number of observations (n) were calculated between the daily OISST and in situ data to compare the two datasets. Moreover, the bias between OISST and in situ data was also calculated to determine the error in OISST. Generally, each in situ SST data is compared with simultaneous OISST grid that contains in situ positions (hereafter called matched OISST data).

To extract the OISST data at the in situ positions, the OISST grid that contains in situ positions was chosen. If the OISST data was missing at the in situ location, then the nearest OISST was chosen.

Finally, a direct comparison was performed between two samples; the first sample includes in situ SST data, however, the second sample includes simultaneous matched OISST data.

2.3. Statistical methods for studying recent Red Sea SST characteristics

The present study employs five statistical methods steps for studying recent Red Sea SST characteristics as follows:

I. The OISST daily dataset was used to describe the spatial and temporal SST variability in Red+ over a 35-year period focusing on seasonal and annual variability.
   - The annual mean (from 1982 to 2016) SST refers to the average of daily OISST data for the 1982–2016 period. However, the annual mean SST refers to the average of daily OISST for a specific year. Moreover, the minimum (maximum) annual mean SST refers to the annual mean SST during the coldest (warmest) year.
   - The annual linear trend (from 1982 to 2016) were calculated using the ordinary least squares estimation of daily OISST data.
   - All the previous calculations were done for each grid, then averaged spatially for each subbasin and the entire study area. Thus:
     - The spatially annual mean (from 1982 to 2016) SST over Red+ refers to spatially averaging of the annual mean (from 1982 to 2016) SST for each grid over Red+.
     - The spatially annual warming trend (from 1982 to 2016) over Red+ refers to spatially averaging of the annual warming (from 1982 to 2016) for each grid over Red+.

- The spatially annual standard deviation (from 1982 to 2016) SST over Red+ refers to spatially averaging of the standard deviation (from 1982 to 2016) SST for each grid over Red+.

II. HYCOM's daily surface currents were used to calculate seasonal and annual averaged surface current over Red+ for the 2007–2016 period. This calculated seasonal and annual averaged surface current was used to elaborate on the SST spatial and temporal dynamics.

III. Seasonality and time lag over the most significant Red+ SST cycle were studied using Fourier analysis based on the daily OISST dataset by calculating the amplitude and phase angle of a one-year cycle to each grid (i, j) as follows:

$$f_{i,j}(t) = ao_{i,j} + \sum_{n=1}^{N} an_{i,j} \cos\left(\frac{2\pi nt}{T}\right) + \sum_{n=1}^{N} bn_{i,j} \sin\left(\frac{2\pi nt}{T}\right), \quad (1)$$

where T is the one-year period, and t is the time; when the seasonal cycle is predominant, only the terms up to $n = 1$ can be retained and the Fourier analysis becomes

$$f_{i,j}(t) = ao_{i,j} + a1_{i,j} \cos\left(\frac{2\pi t}{T}\right) + b1_{i,j} \sin\left(\frac{2\pi t}{T}\right) = ao_{i,j} + A_{i,j} \cos\left(\frac{2\pi t}{T} - \vartheta_{i,j}\right), \quad (2)$$

where ao, $a1$ and $b1$ are the Fourier coefficients

$$ao = \frac{1}{T}\int_{-T/2}^{T/2} f(t)\,dt,$$

$$a1 = \frac{2}{T}\int_{-T/2}^{T/2} f(t)\cos\left(\frac{2\pi t}{T}\right)dt,$$

$$b1 = \frac{2}{T}\int_{-T/2}^{T/2} f(t)\sin\left(\frac{2\pi t}{T}\right)dt$$

and

$$A\ (\text{Amplitude}) = \sqrt{a1^2 + b1^2} \text{ and } \vartheta\ (\text{phase lag}) = \tan^{-1}\frac{b1}{a1}.$$

IV. The monthly and interannual effects of various atmospheric parameters, i.e., T_{2m}, SLP, TCC, τ_{ac} (cross-coast surface wind stress), τ_{al} (cross-coast surface wind stress), air-sea heat fluxes, AMOI, NAOI and ISMI, on SST variability were studied using the correlation coefficient (R) and the number of observations (n).

ERA-Interim surface wind data are available only in the form of zonal and meridional wind speed at a 10-m height; thus, the τ_{ac} and τ_{al} were calculated as follows:

- Eastward wind stress (τ_{ax}) and northward wind stress (τ_{ay}) were calculated from the wind components at 10 m above sea level (zonal and meridional wind components) using a standard bulk formula with a calculation of the air drag coefficient from its nonlinear form (Large and Pond, 1981) and with a modification for low wind speeds (Trenberth et al., 1990).
- τ_{ac} and τ_{al} were calculated from τ_{ax} and τ_{ay} using the coastal orientation (θ) as follows:

$$\tau_{al} = \tau_{ax}\cos(\theta) - \tau_{ay}\sin(\theta), \quad (3)$$

$$\tau_{ac} = \tau_{ax}\sin(\theta) + \tau_{ay}\cos(\theta). \quad (4)$$

In general, the air-sea heat fluxes were defined by the net heat loss from the sea (F_n) and solar radiation to the open water surface (Fsw), where

$$F_n = \text{sensible heat flux } (F_h) + \text{latent heat flux } (F_e) + \text{net longwave radiation } (F_l). \quad (5)$$

V. Principal component analysis (PCA) was applied to 13 daily variables (SST, T_{2m}, SLP, TCC, τ_{ac}, τ_{al}, F_e, F_l, F_h, F_n, Fsw, NAOI and ISMI) from 1982 to 2016 to interpret the linear combination between them. PCA is an unsupervised mathematical method to replace original variables by a much smaller number of uncorrelated variables called principal components (PC). The first PC is dominated by the variable with the largest variance, the second PC is dominated by the variable with the second largest variance, and so on. The computation of principal components is fully described by Jolliffe (2002).

In this study, Red+ is divided into four subbasins: GOA, SRed, CRed, and NRed. All correlation coefficients and linear trends have been tested for significance at the 95% level.

2.4. Heat waves and chlorophyll-*a*

Heat waves are typically defined as three consecutive hot days (a hot day is determined by the temperature exceeding the summer mean plus twice the summer standard deviation). Heat waves are calculated to evaluate the effect of recent warming trends on marine biota, especially when their thermal limits may be approached or exceeded (Chaidez et al., 2017). The Red Sea was divided into a number of clusters to study heat wave characteristics in each cluster.

Clustering of daily SST was performed to classify Red+ into several clusters. A cluster contains a number of grids that are more similar between themselves than to any grids not in the cluster. The k-means clustering algorithm depends on calculating the distance between each object in the dataset to the center of each cluster (k) as described in MacQueen (1967). Clearly, the distance calculation together with a specific number of clusters play a vital role in the algorithm. In the current paper, the correlation, mean and geographical position were used for distance calculations in the k-means algorithm.

The current calculation was designed to: (1) run k-means clustering algorithm (mean is the distance measured) for several iterations with increasing k; (2) choose the best iteration based on each cluster that contains grids with a range of 0.4°C; (3) calculate the correlation coefficient between each grid and the other grids in the same cluster and remove the grids that describe a low correlation ($R < 0.95$) with the other grids from the cluster; (4) remove from the cluster the grids that lie on abnormal geospatial

distance from other grids in the same cluster; and (5) repeat the steps 1 to 4 only for the removed grids (according to correlation or geospatial distance) to classify new clusters.

To understand the effect of heat waves on the Red Sea, the effect of heat waves on chl-a concentrations was analyzed for each cluster.

2.5. Projected Red+ Tos for the 21st century using the GFDL model result

GFDL model simulation databases were used to simulate projected sea surface temperature (Tos) under three different simulations. The GFDL-ESM2M simulation is the result of a system of coupling different models: AM2 (Anderson et al., 2004) for the atmospheric component, LM3 for the land component (Anderson et al., 2004; Milly et al., 2014), and the Modular Ocean Model, version 4p1 (MOM4p1) for sea ice and ocean content (Griffies, 2009). The GFDL-ESM2G simulation, unlike the GFDL-ESM2M simulation, employs the Generalized Ocean Layer Dynamics (GOLD; Adcroft and Hallberg, 2006) model for ocean components instead of MOM4p1. The GFDL-CM3 simulation is intended to improve on GFDL-ESM2M by using AM3 (Donner et al., 2011) for the atmospheric component, LM3 (Milly et al., 2014) for the land component, the sea ice simulator (SIS) for the ice component (Griffies et al., 2011) and MOM 5 for the ocean components (Griffies et al., 2011).

The Tos results from the three different GFDL model simulations (i.e., CM3, ESM2G and ESM2M) under the four RCP scenarios for the 2006–2010 period was tested using OISST SST data. The GFDL model ensemble mean for these three simulations was also calculated. Direct annual biases (Tos minus SST) were calculated for the four simulations to evaluate their performance in describing the current Red+ SST. Only the simulations that realistically describe the current SST were used to project Tos through 2100.

Future Tos trends and uncertainties under the four RCP scenarios were calculated using the 30-year running average. In the current research, there are four sources of uncertainty, which are associated with the scenario design, the model simulation, and seasonal and regional variations.

3. Results and discussion

3.1. In situ SST and OISST data sets

In this section, the feasibility of using OISST datasets in describing the Red+ sea surface temperature is investigated by determining the direct correlation and bias between OISST and in situ SST.

In situ data cover the period from 1982 to 2012, as shown in Fig. 2a, most markedly collecting data during 2007; however, in situ data cover Red+ most markedly in NRed (Fig. 2b). In situ data cover both coastal and open water areas.

The daily OISST data adequately follow the in situ data at a 99% significance level ($R = 0.98$, $n = 53{,}682$). The average bias (OISST, in situ) is -0.2°C. OISST data shows a bias range from -0.3°C to 0.3°C in 65% of the in situ data, as shown in Fig. 3. Thus, OISST data can be used to study the local features of Red+.

3.2. Spatial/temporal distribution of Red Sea surface temperature

It is clear from Figs. 4 and 5 that the annual mean (from 1982 to 2016) SST in Red+ reaches its maximum value over grids concentrated in SRed and is associated with the surface current system. From autumn to spring, the maximum SST occurred along the southeastern Red Sea coast from 15°N to 18°N. This finding can be explained by the fact that the SRed surface water is significantly influenced by the surface flow from the Gulf of Aden (which has a lower SST than SRed). Most of the GOA surface water inflow passes through the western part of SRed, leading to a significant moderating process along the southwestern coast of SRed in comparison to the southeastern coast of SRed as seen in Fig. 5. During the summer season, the maximum SST occurred along the southwestern coast from 14°N to 16°N. The water in SRed is influenced by the water flows from CRed (which has lower SST than SRed) that pass along the southeastern coast and moderate its SST. However, the southwestern coast is not influenced by the water flows from CRed (Fig. 5d).

The annual mean (from 1982 to 2016) SST in Red+ reaches its minimum values (22.5°C) over grids concentrated in the Gulf of Suez as shown in Fig. 5a. The SST in the Gulf of Suez is colder than that in the Gulf of Aqaba, which is at the same latitude, most markedly in summer. This finding is due to the shallow water characteristics of the Gulf of Suez. Moreover, a cyclonic gyre in NRed inducing more flow of relatively warmer Red Sea surface water to the Gulf of Aqaba results in an increase of the Gulf of Aqaba SST compared to the Gulf of Suez.

The Red Sea SST temporal variation from 1982 to 2016 is described in terms of the means of the seasonal and annual cycle, while its spatial variation treats Red+ as four subbasins (the Gulf of Aden, SRed, CRed, and NRed). The spatially annual mean (from 1982 to 2016) SST over Red+ is $27.88 \pm 2.14^{\circ}$C (Fig. 4a and Table 1). In addition, the Red Sea SST increased meridionally from south to north, partly due to the amount of absorbed solar energy. However, GOA is colder than SRed, due to the moderation process in GOA resulting from the upwelling process in GOA during the Indian summer monsoon (Bower and Furey, 2012; Wilson and Rebecca, 2000) together with the exchange with relatively cold water from the Arabian Sea (northern Indian Ocean). Moreover, the maximum value of annual mean (from 1982 to 2016) SST across Red+ shows a significant variation with latitude (data are not shown), where this value ranges from 34.92°C at 16° latitude to 29.06°C at 30° latitude. This result agrees with Chaidez et al. (2017) and Karnauskas and Jones (2018).

Moreover, grid to grid correlation between the annual mean (from 1982 to 2016) from one side and the four different seasons from the other side is used to quantify the similarities between their SST patterns. Autumn, winter and spring mean (from 1982 to 2016) SST patterns are quantitatively close to the annual (from 1982 to 2016) pattern with correlation coefficients of 0.9, 0.87 and 0.86 respectively ($n = 1119$). However, the summer mean (from 1982 to 2016) SST pattern is the quantitatively least close to the annual pattern ($R = 0.71$, $n = 1119$). This result indicates that the mean summer SST pattern significantly differs from the other three seasonal patterns, supporting the previous finding of Karnauskas and Jones (2018), while

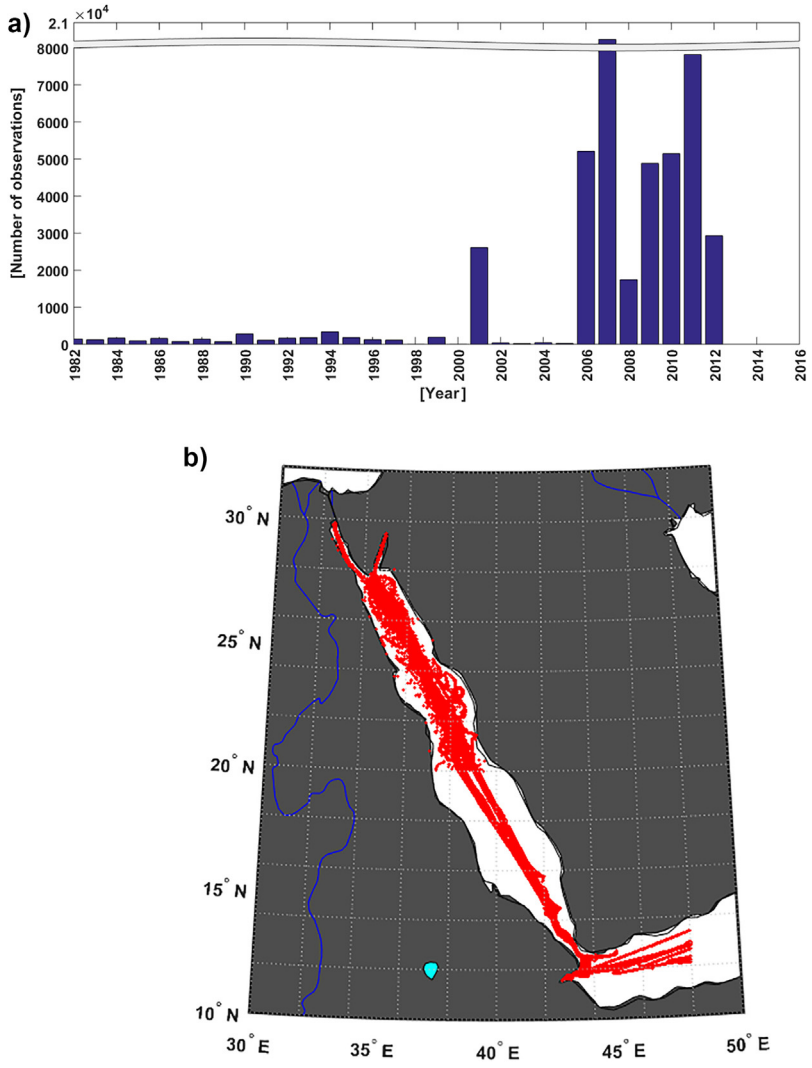

Figure 2 Temporal (a) and spatial (b) distribution of the in situ data. *y*-axis break is used to improve visualization of the plot (a).

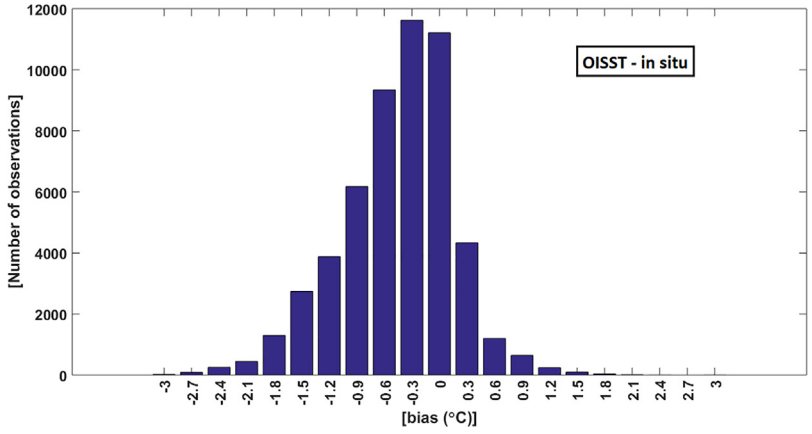

Figure 3 Histogram of the difference between satellite data and in situ data. Positive values represent a warm bias in the OISST data with respect to in situ data.

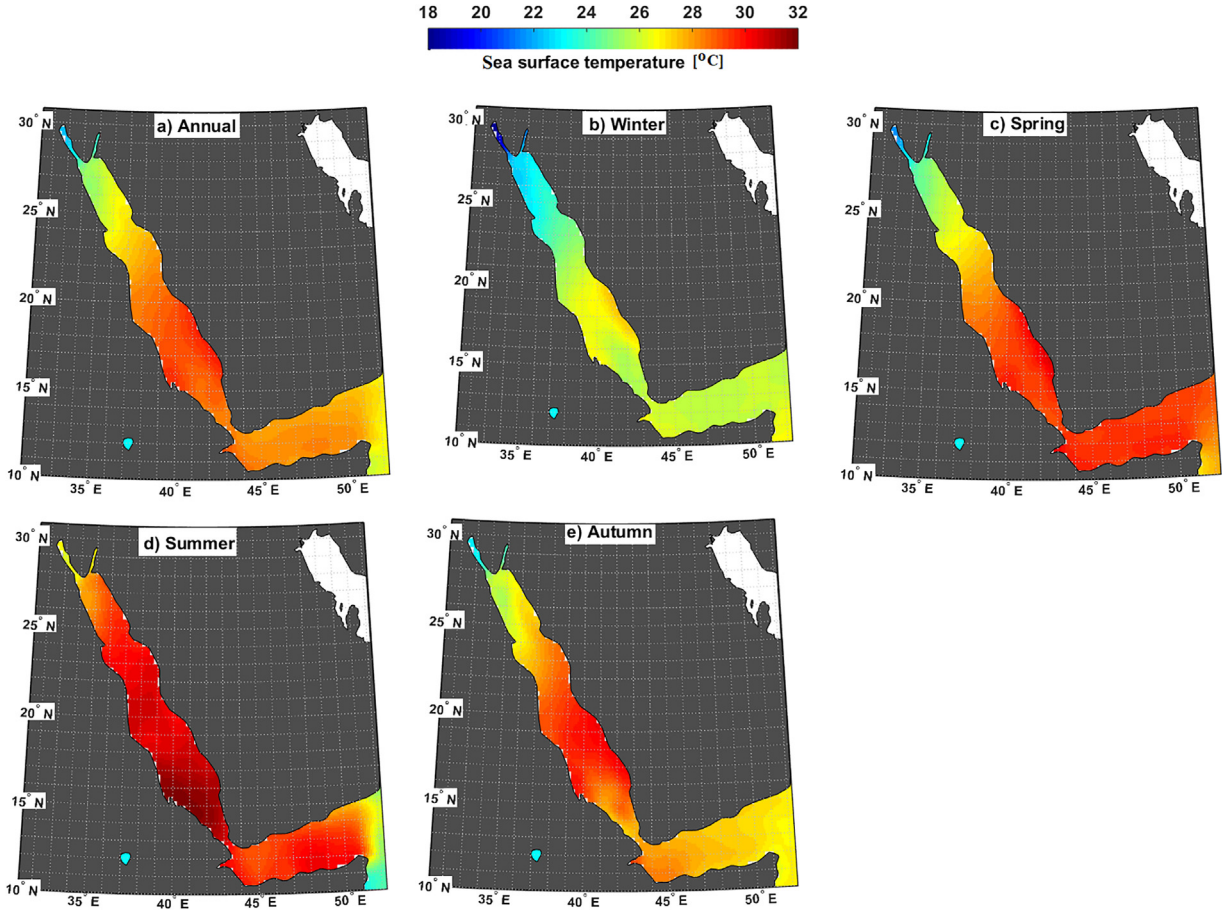

Figure 4 Spatial distribution of the mean annual/seasonal Red+ SST over the period from 1982 to 2016.

improving the analysis from qualitative to quantitative and including autumn/spring seasons.

The spatially annual standard deviation (from 1982 to 2016) based on daily SST ranges from 1.55°C in GOA to 2.42°C in NRed. This gradient of the variability is relatively higher during summer than winter in GOA, SRed, and NRed, whereas in CRed, the variability is relatively higher during winter than summer (Table 1). Although the previous finding of Karnauskas and Jones (2018) showed that the standard deviation is relatively higher in winter than summer, the current research shows that the standard deviation in the Red Sea shows similar values (=0.62°C) during winter and summer. This disagreement with Karnauskas and Jones (2018) is probably because the current research uses daily SST data in the calculation, while Karnauskas and Jones (2018) used monthly SST. In addition, the current research provides more details about the variations between the four Red+ subbasins.

Generally, OISST data show a significant seasonal range of 4.2°C and 5.1°C in the Red+ and the Red Sea, respectively (Table 1). This seasonal range in the Red Sea is less than the value previously calculated by Berman et al. (2003), due to the longer study period in the current research.

Fig. 6 shows that the SST in NRed is colder than in the other three zones. The highest percentages of SST occurrences are 26°C, 30°C, 30°C and 24°C in the Gulf of Aden, SRed, CRed, and NRed, respectively. For the highest SST (>30°C), the percentages of occurrences are 16.3%, 42%, 30% and 7.5% in the Gulf of Aden, SRed, CRed, and NRed, respectively. Although GOA receives much amount of insolation in comparison to SRed and CRed, GOA showed a lower occurrence of the highest SST. This finding indicates a more intensive cooling process resulting from the upwelling process during the Indian summer monsoon that dominates in GOA. On the other hand, for the lowest SST (<24°C), the percentage of occurrences are 0.95%, 0.09%, 2% and 25.8% in the Gulf of Aden, SRed, CRed, and NRed, respectively.

The annual SST warming trends (from 1982 to 2016) in Red+ (Fig. 7 and Table 1) range from 0.034°C yr^{-1} over grids concentrated in NRed to 0.017°C yr^{-1} over grids concentrated in the Gulf of Aden, with average values of 0.025 $\pm$ 0.006°C yr^{-1}. The semi-enclosed nature of NRed is responsible for its intensive warming trend (Belkin and Rapid, 2009); however, the upwelling process and exchange with the Indian Ocean explain the slowed warming in GOA.

The Red Sea warming trend (from 1982 to 2016) is approximately 2.6-times higher than the global ocean warming trend from 1980 to 2005 (=0.011°C yr^{-1}, IPCC (2014)). Cantin et al. (2010) noted that the highest warming trend occurred in CRed, which counters the current finding due to the calculations based on different time scales and the more accurate SST database used in the current research. Moreover, the warming rate of the Red Sea is higher than that previously estimated (=0.017°C yr^{-1}) by Chaidez et al. (2017), because the current study uses the average daily temperature in trend

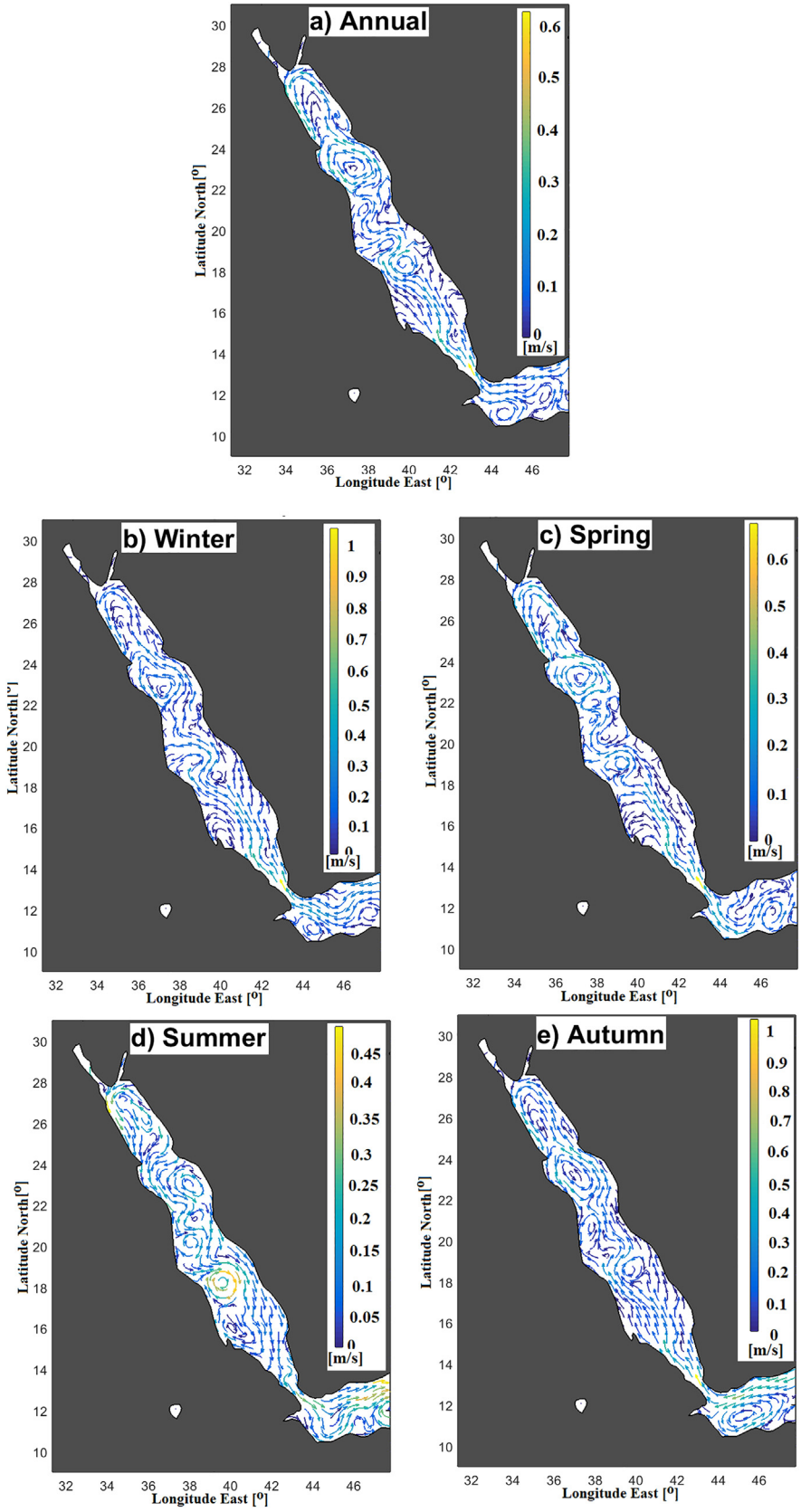

Figure 5 Annual/seasonal surface Red+ current over the 1993–2016 period, calculated from the HYCOM database output for the 2007–2016 period.

Table 1 Daily sea surface temperature characteristics (mean, minimum, maximum and trend) in the studied subbasins from 1982 to 2016 (the linear trends were tested using a t-test at a 99% significance level for significance). Light gray rows indicate summer, while dark gray rows denote the winter season. All the calculations used daily OISST daily data.

	Red+	GOA	Red Sea	SRed	CRed	NRed
Spatially mean (from 1982 to 2016) ± standard deviation [°C]						
Annual	27.84 ± 1.78	27.78 ± 1.55	27.88 ± 2.14	29.03 ± 2.13	28.43 ± 2.02	26.06 ± 2.42
Winter	25.44 ± 0.52	25.93 ± 0.69	25.11 ± 0.62	26.26 ± 0.61	25.80 ± 0.78	23.15 ± 0.79
Spring	28.35 ± 1.12	29.21 ± 1.04	27.78 ± 1.27	29.44 ± 1.25	28.22 ± 1.21	25.52 ± 1.51
Summer	29.62 ± 0.49	28.63 ± 0.74	30.28 ± 0.62	31.26 ± 0.65	30.53 ± 0.69	28.95 ± 0.85
Autumn	27.91 ± 1.31	27.35 ± 1.09	28.29 ± 1.51	29.13 ± 1.73	29.12 ± 1.41	26.55 ± 1.54
Minimum of spatially mean [°C] (year)						
Annual	27.27 (1984)	27.05 (1984)	27.25 (1992)	28.42 (1984)	27.68 (1992)	25.16 (1983)
Winter	24.72 (1992)	25.03 (1984)	24.00 (1992)	25.39 (1992)	24.39 (1992)	22.08 (1992)
Spring	27.64 (1982)	28.63 (1984)	26.93 (1982)	28.65 (1982)	27.21 (1982)	24.67 (1983)
Summer	28.87 (1984)	27.47 (1984)	29.44 (1991)	30.38 (1984)	29.63 (1991)	27.87 (1983)
Autumn	27.29 (1984)	26.53 (1984)	27.65 (1985)	28.23 (1991)	28.43 (1985)	25.83 (1993)
Maximum of spatially mean [°C] (year)						
Annual	28.47 (2010)	28.29 (2015)	28.59 (2010)	29.64 (2016)	29.06 (2016)	27.20 (2010)
Winter	26.16 (2016)	26.78 (2016)	25.96 (2010)	27.20 (2016)	26.74 (1999)	24.66 (2010)
Spring	29.20 (2016)	30.07 (2010)	28.86 (2016)	30.18 (2016)	29.40 (2016)	26.86 (2016)
Summer	30.17 (2001)	29.55 (2015)	31.01 (2001)	32.04 (2001)	31.39 (2001)	29.72 (2012)
Autumn	28.66 (2010)	28.32 (2015)	29.25 (2010)	30.05 (2015)	30.05 (2010)	28.12 (2010)
Spatially trend (from 1982 to 2016) [°C yr^{-1}]						
Annual	0.025	0.017	0.029	0.026	0.028	0.034
Winter	0.021	0.012	0.027	0.022	0.032	0.027
Spring	0.022	0.014	0.027	0.022	0.027	0.034
Summer	0.020	0.014	0.024	0.021	0.018	0.034
Autumn	0.025	0.026	0.024	0.025	0.020	0.026

calculations, while Chaidez et al. (2017) used the maximum daily temperature in trend calculations. The Red Sea spatially annual warming trend is not uniform throughout the study period, ranging from 0.056°C yr^{-1} in the 2005–2016 period, to 0.051°C yr^{-1} in the 1994–2005 period and to 0.040°C yr^{-1} in the 1982–1993 period, indicating that the warming trends have become more intense over time in the Red Sea.

There is a significant seasonal average warming trend (from 1982 to 2016) in Red+, ranging from 0.025°C yr^{-1} during autumn to 0.020°C yr^{-1} during summer. The annual warming trend (from 1982 to 2016) in NRed is concentrated during spring and summer. However, the annual warming trend dominated during winter in CRed and during autumn in GOA/SRed. The Gulf of Aden's warming trend is less significant than SRed's warming trend over the entire year, except during autumn; the Gulf of Aden's warming trend is more intensive than that in SRed. Moreover, the warming trend in the Gulf of Aqaba is more intensive than that in the Gulf of Suez, indicating that the SST difference between the two Gulfs may increase in the future.

3.3. Variability of Red Sea surface temperature

The Fourier analysis of 35 years of daily Red+ SST indicates that the annual SST cycle is the most significant. There is an obvious SST seasonality variation (Fig. 8) ranging from its maximum amplitude (5°C) in the Gulf of Suez to its minimum amplitude (less than 2°C) in the Gulf of Aden together with the zone that extends from 17° latitude to 21° latitude. The SST seasonality is much higher in northern Bab el-Mandeb Strait in comparison to the southern part, partly due to the moderate SST effect in the Gulf of Aden. Moreover, SST seasonality is much higher in the Gulf of Suez in comparison to the same latitude in the Gulf of Aqaba, where the Gulf of Aqaba has a similar SST seasonality (approximately 3°C) as the northern part of NRed.

The seasonality of the Red+ SST phase lag displays a mix of zonal/meridional variation ranging from its minimum value (nearly −110 days) in the GOA to its maximum (nearly −150 days) value off Al Lith (lies along the Saudi Arabian Red Sea coast at approximately 20° latitude). This finding indicates that the seasons begin earlier in GOA where the maximum SST occurred around July 20th, while the seasons come later off Al Lith where the maximum SST occurred around August 29th (i.e., there is an obvious seasonal shift in Red+ by approximately 40 days). The current analysis supports the previous finding of Chaidez et al. (2017), who stated that the maximum time delay for the maximum SST in the Red Sea occurred off the Al Lith coast from mid-August to early September using normal analysis of daily maximum SST.

The phase lag distribution of the annual SST signal exhibits a zonal pattern in GOA, followed by a meridional pattern in SRed until 18° latitude. This finding can be explained by the surface current system (Fig. 5). From 18° to 28° latitude, the phase lag of the annual SST signal distribution decreases zonally from east (−150 days) to west (−140 days) following the cyclonic gyre system in the study area.

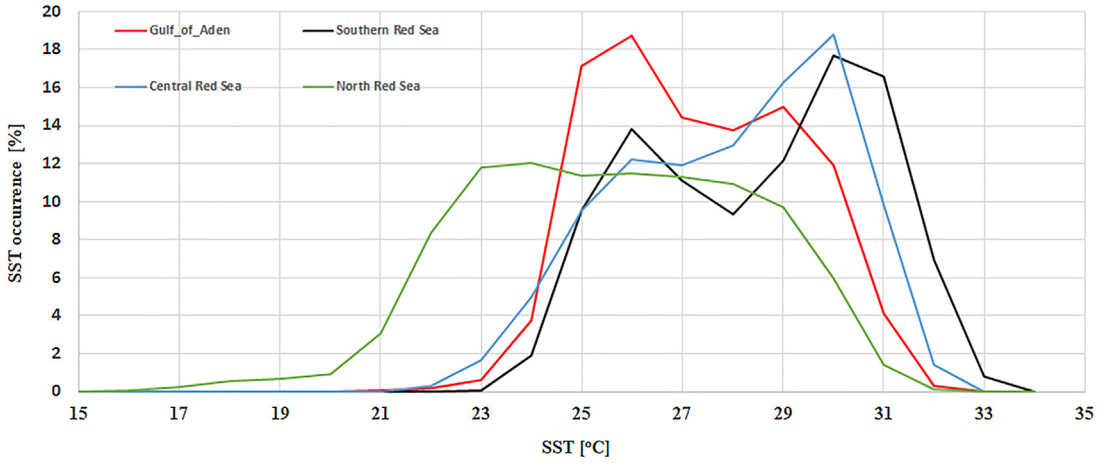

Figure 6 Occurrence percentage of the sea surface temperature in the four studied subbasins over the period from 1982 to 2016.

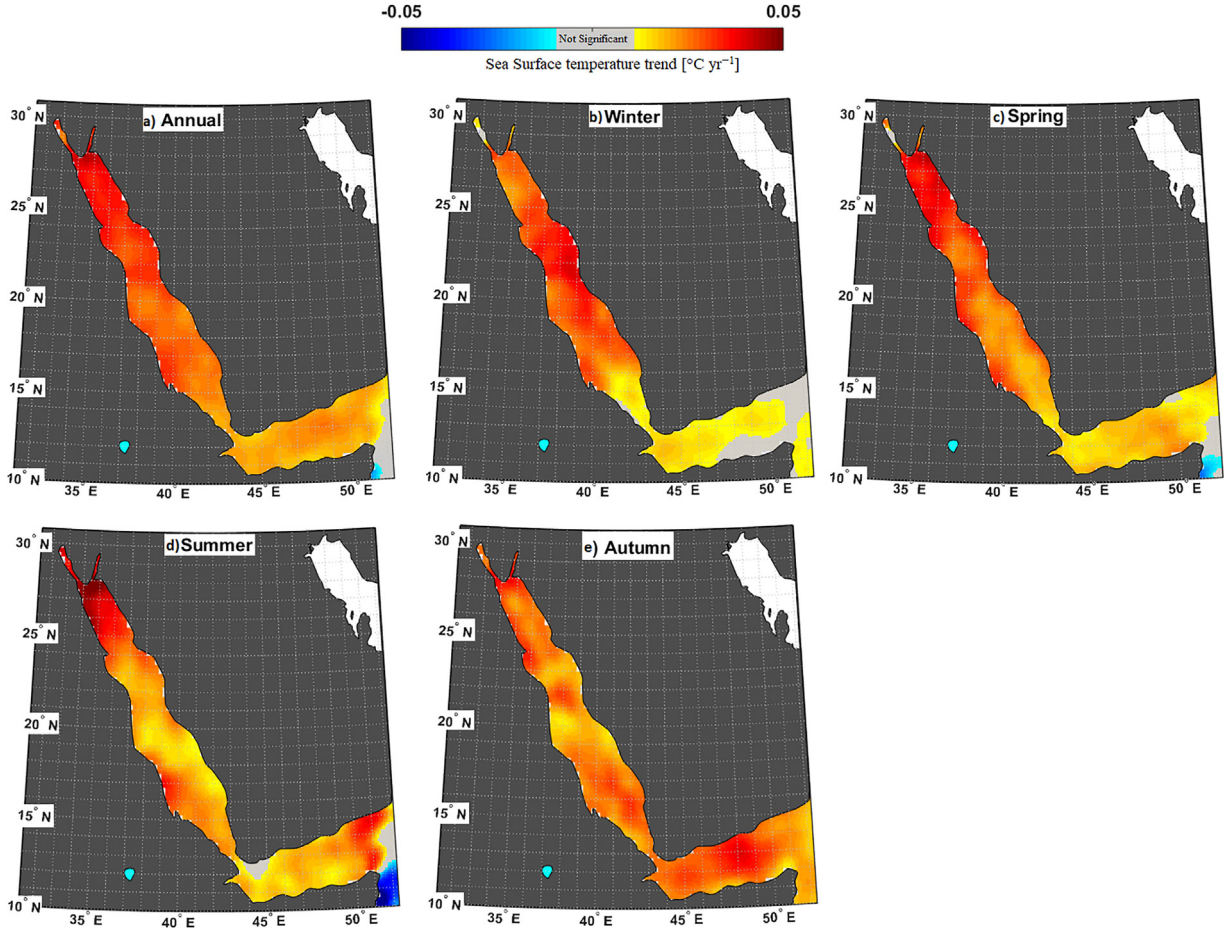

Figure 7 Spatial distribution of the annual/seasonal Red+ SST trends over the period from 1982 to 2016.

3.4. Correlation between the ten studied atmospheric parameters and the Red Sea surface temperature

Previous studies suggest that the ten studied atmospheric parameters have relationships with SST. The features of these relationships in Red+ were evaluated using correlation coefficients to provide insightful information about different atmospheric phenomena that are associated with changing SST. For example, these relationships should be considered for designing a simple model of Red+.

In general, the Red+ SST is negatively correlated with SLP, F_n, and NAOI. The Red+ SST, however, is positively correlated with T_{2m}, Fsw, AMOI, and ISMI. In addition, TCC, τ_{ac}, and τ_{al}

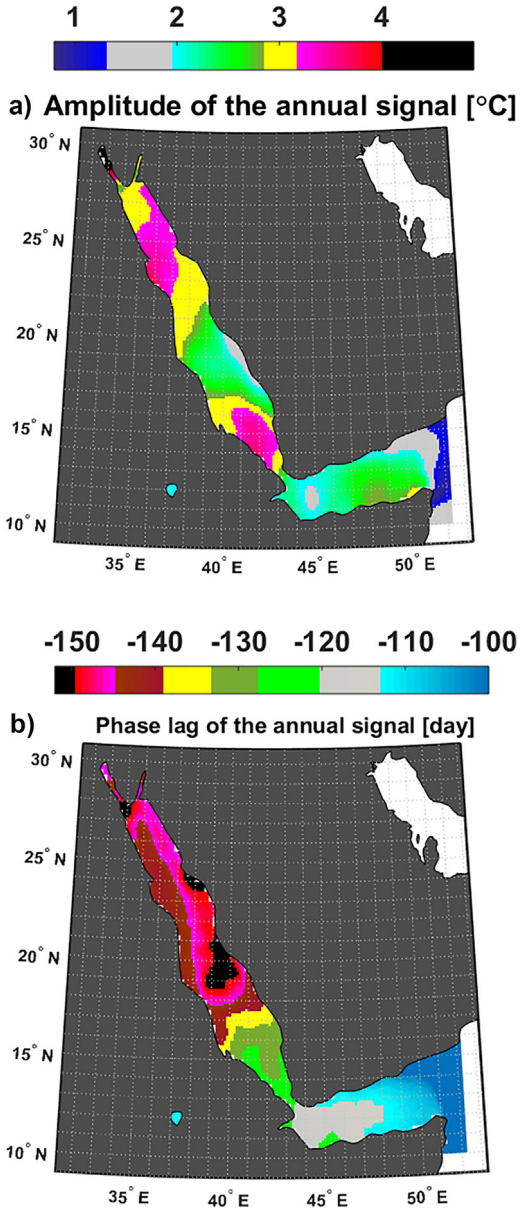

Figure 8 Spatial distribution of the amplitude (a) and phase lag (b) of the annual Red+ SST signal over the period from 1982 to 2016.

have spatially varying correlations, either positive or negative (Fig. 9).

The monthly correlation coefficient (R) between SLP and SST in Red+ has an average value of −0.75 (n = 420), with a markedly low value in CRed. There is a significant seasonal variation in the correlation between SST and SLP, ranging from the maximum values (R = −0.89, n = 105) during autumn to the minimum values (R = 0.14, n = 105) during summer. Only during summer does the monthly correlation between SLP and SST exhibit a significant positive correlation in 30% of Red+, most markedly off Al Lith and to the north and south of Bab el-Mandeb Strait (data are not shown). This significant positive correlation indicates that the processes controlling the relationship between SST and SLP (e.g., atmospheric stability and circulation and thermal conditions) are quite different in summer than in the other seasons. You et al. (2017) stated that SST could exhibit a positive correlation with SLP in a season under considerable conditions (e.g., during the winter season in the Tibetan Plateau).

Monthly correlation analysis between SST and TCC shows three patterns in Red+; the first pattern is at 22° latitude and has a strong negative correlation; the second pattern is from 12° to 16° latitude and has a strong positive correlation, and the third pattern is concentrated in CRed and GOA where the correlation is not significant. The negative correlation suggests that the cloud cover affects SST with negative radiative forcing; however, the positive correlation suggests that SST has a significant effect on day-to-day cloud formation and no significant impact on the radiation balance. The correlation between SST and TCC reaches its maximum value during the autumn season.

The monthly correlation coefficient between SST and τ_{ac} generally shows a strong positive correlation in NRed, CRed and GOA, while the correlation shows a strong negative relationship in the southern part of the Red Sea (northern and southern Bab el-Mandeb Strait). There is no significant correlation between SST and τ_{ac} in the borders between areas of negative and positive correlation.

The monthly correlation coefficient between SST and τ_{al} generally shows a strong positive correlation in SRed and in GOA related to the monsoonal forcing of a long-basin wind in SRed, while the correlation shows a moderate negative correlation in NRed. There is no significant correlation between SST and τ_{al} in CRed. These positive and negative correlations occurred when the surface current moves parallel to the coastline toward the north or the Indian Ocean, respectively, as seen in Fig. 5. It can be concluded that the wind direction drives the correlation between SST and τ_{ac}/τ_{al} to be positive or negative.

Direct correlation analysis between SST and wind speed was then carried out to show the relationship between SST and wind speed (Fig. 10). In general, SST and wind speed are negatively correlated (R = −0.47, n = 420), which supports the previous finding of Qu et al. (2012). This result is explained by the fact that increasing wind speed affects seawater stratification and raises subsurface water. Moreover, Wang et al. (1999) showed that increases in surface wind speed are associated with more evaporation and a surface cooling process, which leads to an additional increase in surface wind speed and vice versa (i.e., there is a feedback system between surface wind, evaporation, and SST). The correlation between SST and wind speed shows a strong seasonal variation ranging from R = −0.6 (n = 105) during autumn, to R = −0.5 (n = 105) during winter and finally to a very low value with no significant correlation during summer and spring, indicating that the difference between SST and T_{2m} plays a significant role in this seasonal variation between SST and wind speed. The significant negative correlation between SST and wind speed during cold seasons supports the previous findings of Samelson et al. (2006). Moreover, Samelson et al. (2006) indicate that during warm seasons, the correlation between SST and wind speed shows a strong positive correlation. This result runs counter to the current finding such that correlation between SST and wind speed is not significant during warm seasons, due to the low wind speed characteristics in the study area during warm seasons.

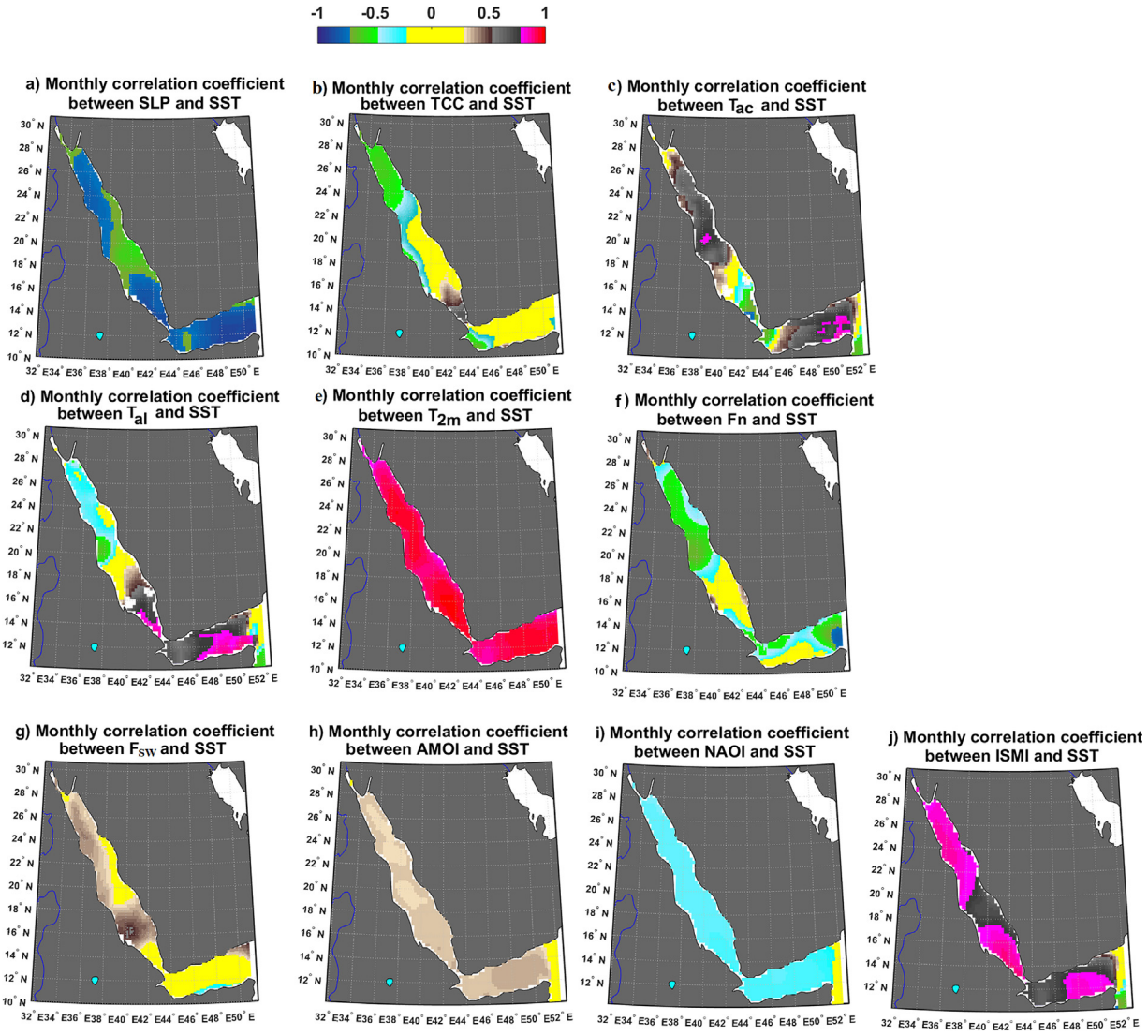

Figure 9 Monthly correlation coefficients between the ten studied atmospheric parameters and the Red Sea surface temperature. Yellow indicates no significant correlation. (For interpretation of the references to color in this figure legend, the reader is referred to the web version of this article.)

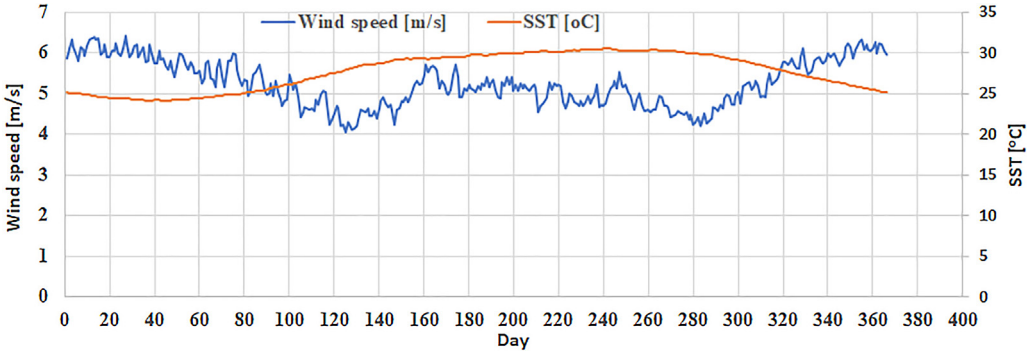

Figure 10 Average daily means of sea surface temperature (SST) and surface wind speed in Red+ over the period from 1982 to 2016.

Table 2a Principal component analysis for the entire study region (Red+) based on the correlation matrix before removing the seasonal cycle. Bold numbers refer to highly significant correlations over 0.30.

Variables	Principal component				
	1	2	3	4	5
Sea surface temperature (SST)	**−0.334**	0.120	0.107	0.160	**0.337**
Mean sea level pressure (SLP)	**0.379**	−0.065	−0.054	0.066	0.059
Air temperature at 2 m above sea level (T_{2m})	**−0.382**	0.079	0.061	0.069	0.193
Total cloud cover (TCC)	−0.014	**0.327**	**−0.511**	−0.233	**−0.569**
Along-coast wind stress (τ_{al})	0.168	**−0.312**	**−0.418**	0.221	0.409
Cross-coast wind stress (τ_{ac})	**0.347**	−0.117	0.057	0.031	−0.031
Latent heat flux (F_e)	0.188	**0.569**	0.187	0.074	0.093
Net longwave radiation (F_l)	0.147	−0.261	**0.567**	0.050	−0.210
Sensible heat flux (F_h)	**0.364**	0.043	0.074	0.029	−0.013
Net heat loss from the sea ($F_n = F_h + F_e + F_l$)	0.266	**0.439**	0.288	0.079	0.034
Solar radiation to the open water surface (Fsw)	0.260	0.313	−0.290	0.179	**0.366**
North Atlantic Oscillation Index (NAOI)	0.106	−0.008	0.069	**−0.902**	**0.396**
Indian Summer Monsoon Index (ISMI)	**−0.332**	0.269	0.095	0.002	0.091

Table 2b Principal component analysis for the entire study region (Red+) based on the correlation matrix after removing the seasonal cycle. Bold numbers refer to highly significant correlations over 0.30.

Variables	Principal component							
	1	2	3	4	5	6	7	8
Sea surface temperature (SST)	0.16	**−0.35**	0.07	**0.50**	−0.03	**−0.43**	−0.11	**0.33**
Mean sea level pressure (SLP)	−0.14	−0.27	**0.45**	0.04	−0.11	0.10	**0.74**	0.02
Air temperature at 2 m above sea level (T_{2m})	**0.41**	−0.04	−0.23	**0.33**	0.03	**−0.36**	0.08	−0.27
Total cloud cover (TCC)	−0.10	**0.43**	0.26	0.22	−0.05	−0.19	−0.18	−0.02
Along-coast wind stress (τ_{al})	**0.39**	0.08	0.09	0.10	−0.05	−0.07	**0.36**	0.08
Cross-coast wind stress (τ_{ac})	−0.12	**−0.37**	**0.38**	0.07	−0.03	−0.06	−0.22	**−0.73**
Latent heat flux (F_e)	**−0.46**	0.10	−0.29	0.23	0.01	−0.16	0.16	−0.19
Net longwave radiation (F_l)	−0.04	**−0.43**	**−0.46**	−0.07	0.03	0.10	0.14	0.12
Sensible heat flux (F_h)	**−0.34**	−0.28	0.29	0.09	−0.04	−0.05	**−0.31**	**0.47**
Net heat loss from the sea ($F_n = F_h + F_e + F_l$)	**−0.48**	−0.05	**−0.33**	0.21	0.01	−0.13	0.14	−0.08
Solar radiation to the open water surface (Fsw)	−0.19	**0.44**	0.13	0.23	−0.07	−0.11	0.22	0.08
North Atlantic Oscillation Index (NAOI)	−0.09	−0.01	0.09	**−0.57**	**0.39**	**−0.70**	0.12	0.04
Indian Summer Monsoon Index (ISMI)	0.01	0.01	0.11	**0.30**	**0.90**	**0.28**	0.03	0.01

There is a strong monthly correlation between SST and T_{2m} in Red+ ($R = 0.92$, $n = 420$), and this correlation ranges from $R = 0.94$ ($n = 105$) during autumn, to $R = 0.91$ ($n = 105$) during spring, to $R = 0.67$ ($n = 105$) during winter and to $R = 0.44$ ($n = 105$) during summer. T_{2m} shows a higher value than SST over the entire year by approximately 0.51°C. This difference shows a significant seasonal variation, where T_{2m} is warmer than SST during summer (1.40°C) and spring (0.94°C) and colder than SST during autumn (0.88°C) and winter (0.87°C). This result can explain the previous finding such that the correlation between wind speed and SST has a significant seasonal variation (during the cold seasons when SST is warmer than T_{2m}, wind speed is inversely proportional to SST, while in the warm seasons when SST is cooler than T_{2m}, wind speed is not significantly proportional to SST).

The monthly net heat loss from the sea (F_n) correlates negatively with the monthly SST ($R = -0.32$, $n = 420$) most markedly in NRed and during winter. However, the monthly solar radiation to the open water surface (Fsw) correlates positively with SST especially between 16°N and 18°N during autumn. Although ERA-Interim used the Monin–Obukhov formulation, which includes SST as an input variable to forecast air-sea heat fluxes, the current analysis used these data set to assess the relative role of air-sea heat fluxes to SST changes in Red+. This procedure followed the previous analysis of He et al. (2017) who studied the correlation between Re-Analysis (ERA-40) and SST in tropical oceans.

The influence of monthly climate indices (AMOI, NAOI, and ISMI) on monthly SST was analyzed spatially (Fig. 9) and temporally. ISMI shows the strongest effect on SST ($R = 0.71$, $n = 420$) compared with the effects of NAOI ($R = -0.33$, $n = 420$) and AMOI ($R = 0.31$, $n = 408$). There is a significant seasonal correlation between SST and NAOI/ISMI peaks in autumn; however, there is no significant seasonal correlation between SST and AMOI.

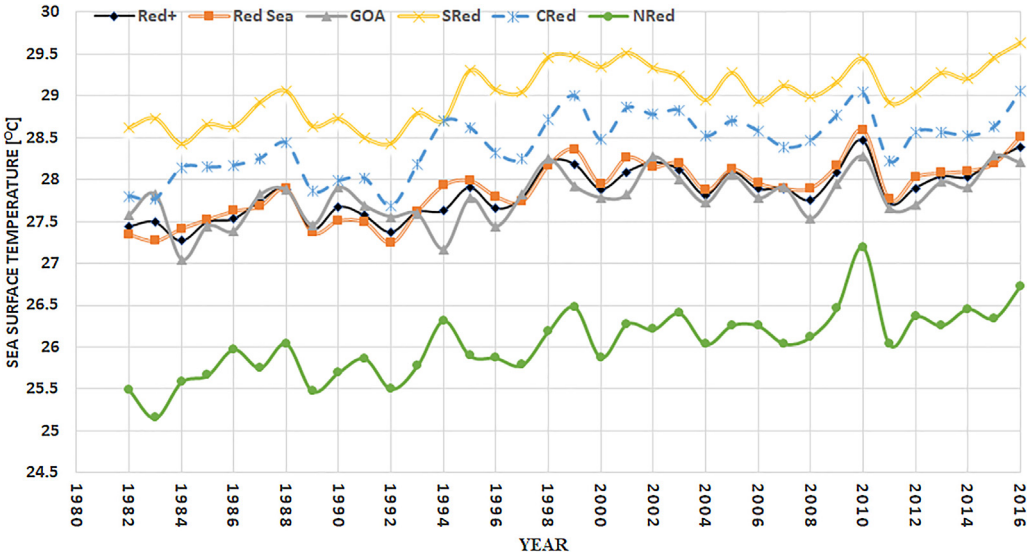

Figure 11 Annual sea surface time series for the studied subbasins. GOA, Gulf of Aden; SRed, Southern Red Sea; CRed, Central Red Sea; NRed, Northern Red Sea; Red+, Red Sea + Gulf of Aden.

With 13 daily variables (SST, T_{2m}, SLP, TCC, τ_{ac}, τ_{al}, F_e, F_l, F_h, F_n, Fsw, NAOI and ISMI) from 1982 to 2016, principal component analysis (PCA) is a meaningful tool to interpret the linear combination between them. PCA reduces the number of variables to a few principal components (Table 2).

PCA shows that only five principal components (PCs) account for 90% of the studied parameter variance in Red+ before removing the seasonal cycle. Their percentages of variance are 48%, 16%, 12%, 8% and 6%. The first PC shows a strong correlation with six of the studied variables. This first PC decreases with SST, T_{2m}, and ISMI but increases with SLP, τ_{ac}, and F_h, indicating that these six variables are highly correlated. The second PC shows a strong correlation with four of the studied variables (increasing with TCC, F_e, and F_n while decreasing with τ_{al}), which similarly indicates that TCC, F_e, F_n, and τ_{al} vary together. The third principal component can be considered a measure of TCC, τ_{al}, and F_l. The fourth principal component, which is responsible for 8% of the overall change in variance in Red+, can be considered a measure of NAOI; additionally, the fifth principal component can be considered a measure of SST, TCC, τ_{al}, Fsw and NAOI, as described in Table 2a.

After removing the seasonal cycle, PCA shows that eight PCs account for 90% of the variance in Red+, and this result is shown in Table 2b. The Fourier analysis technique was used to remove the seasonal cycle.

3.5. Sea surface temperature characteristics in different Red+ subbasins

The spatially annual mean SST (from 1982 to 2016) in Red+ ranges from its maximum value of 29.03 ± 2.13°C in SRed, followed by 28.43 ± 2.02°C in CRed, 27.78 ± 1.55°C in GOA, and 26.06 ± 2.42°C in NRed (Fig. 11 and Table 1). The maximum of spatially annual mean SST in the Red Sea (=28.59°C) occurred during 2010. This finding can be explained by NAOI. In 2010, NAOI showed a dramatic decrease in its positive phase within the studied period. NRed, which is highly correlated to NAOI in comparison to the other studied subbasins, exhibited a 0.72°C increase (1.9 times the Red+ increase) from 2009 to 2010; it was followed by a 1.16°C decrease (1.6 times the Red+ decrease) from 2010 to 2011. On the other hand, the minimum of spatially annual mean SST in the Red Sea (=27.25°C) occurred during 1992 (most notably in CRed). This result agrees with the previous finding of Raitsos et al. (2011), who showed that 1992 was the coldest year for the Red Sea. A comparison between the hottest and coldest years in the Red Sea indicates that the range of the spatially annual mean temperature during the study period is only 1.34°C.

The SST time series analysis of the studied subbasins displays a spatially annual positive trend with varying significance from north to south, in detail, ranging from 0.034°C yr^{-1} in NRed to 0.017°C yr^{-1} in GOA. There is a significant seasonal variation in the spatially seasonal warming trend ranging from 0.027°C yr^{-1} during winter to 0.024°C yr^{-1} during summer and autumn.

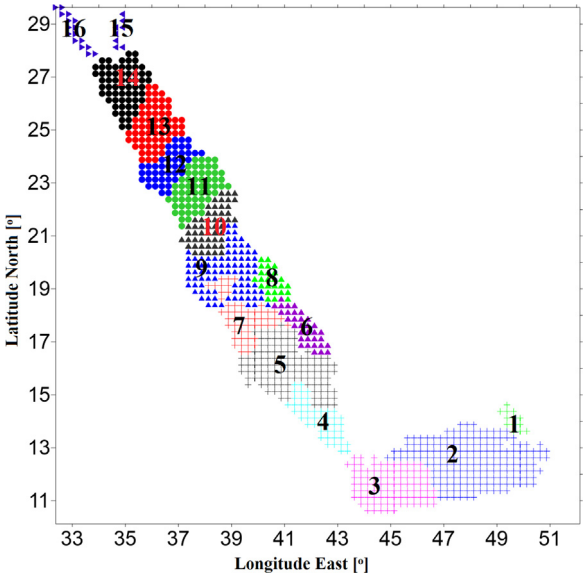

Figure 12 Spatial clustering of SST data (1982–2016) for Red+.

Table 3 Heat wave characteristics. The relationship between heat waves and chl-a concentrations is also shown (NA indicates low-quality calculations of chl-a concentrations in the area).

Cluster number	1982–2016			2003–2016	
	heat wave days [%]	Most pronounced heat wave events	Minimum heat wave temperature [°C]	Average chl-a concentration [mg/m^3] during	
				the entire year	heat wave events
1	0.23	7 days (12/06/1988 to 18/06/1988)	31.46	0.57	0.16
2	0.23	5 days (12/06/1988 to 16/06/1988)	31.98	0.92	0.37
3	0.17	5 days (27/05/2005 to 31/05/2005)	31.94	0.84	0.17
4	0.25	5 days (24/09/1995 to 28/09/1995) (16/09/1998 to 20/09/1998)	33.11		NA
5	0.13	7 days (13/08/2001 to 19/08/2001)	33.20	No heat wave events occurred from 2003–2016	
6	0.31	9 days (7/10/2001 to 15/10/2001)	32.79		NA
7	0.19	6 days (6/10/2002 to 11/10/2002)	32.65	No heat wave events occurred from 2003–2016	
8	0.31	7 days (27/10/2002 to 02/11/2002)	32.51	0.64	0.18
9	0.22	4 days (14/10/2002 to 17/10/2002)	32.36	No heat wave events occurred from 2003–2016	
10	0.34	11 days (03/08/1998 to 13/08/1998)	32.46		NA
11	0.39	14 days (14/07/2001 to 27/07/2001)	32.14	0.21	0.11
12	0.38	13 days (15/07/2001 to 27/07/2001)	31.82	0.16	0.13
13	0.31	11 days (25/08/2003 to 04/09/2003)	31.31	0.16	0.09
14	0.40	10 days (24/07/2007 to 02/08/2007) (18/09/2015 to 27/09/2015)	30.43	0.17	0.12
15	0.50	18 days (29/07/2012 to 15/08/2012)	29.02	0.30	0.14
16	0.42	9 days (22/08/1995 to 30/08/1995) (26/07/2007 to 03/08/2007)	28.07	0.35	0.20

Moreover, a cross-correlation among the 4 subbasins annual time series was used to quantify the similarities between different subbasins. The spatially annual SST variation in GOA is relatively different than those in SRed ($R = 0.56$, $n = 35$) and CRed ($R = 0.55$, $n = 35$). Moreover, the spatially annual SST variation in CRed is much closer to the SRed pattern ($R = 0.86$, $n = 35$) than to NRed ($R = 0.73$, $n = 35$). In general, the spatially annual SST variation in the Red Sea is much closer to the CRed spatially annual SST pattern ($R = 0.98$, $n = 35$).

3.6. Heat waves and chlorophyll-*a*

To understand the Red+ heat waves, cluster analysis was conducted to divide Red+ into 16 clusters (Fig. 12). Each cluster contains a number of grids that have a correlation over 0.95 between themselves and a range of 0.4°C together with minimum distance (clustering was performed using daily SST for the entire data series). The cluster regime runs generally from east to west across the Gulf of Aden and runs from south to north in the Red Sea.

Heat waves were considered at least three days with hot SST. A day was considered a hot day with an SST equal to or higher than two standard deviations plus the mean SST of the hottest month within each cluster. This method indicates that the heat wave minimum temperature varies from one cluster to another (Table 3) and ranges from 33.2°C in cluster 5 to 28.07°C in cluster 16 (the Gulf of Suez). Red+ experiences heat waves for approximately 0.30% of the year, most pronounced in cluster 15 (the Gulf of Aqaba) and least pronounced in cluster 5. The most pronounced Red+ heat waves events occurred for

Table 4 Performance of various GFDL simulations (CM3, ESM2M and ESM2G) in the Red Sea during the control period (2006–2016). GFDL model ensemble mean = ensemble mean of all 3 GFDL simulations. The shaded column shows the best performing simulation.

Simulation	Scenario	Subbasin	Annual (Tos-SST)	Simulation	Scenario	Subbasin	Annual (Tos-SST)
GFDL-CM3		Red+	0.30			Red+	−0.72
	RCP2.6	Red	0.55		RCP2.6	Red	−0.67
		GOA	−0.23			GOA	−0.82
		Red+	0.25			Red+	−0.81
	RCP4.5	Red	0.53		RCP4.5	Red	−0.77
		GOA	−0.34			GOA	−0.90
		Red+	0.05	GFDL-ESM2M		Red+	−0.86
	RCP6.0	Red	0.31		RCP6.0	Red	−0.80
		GOA	−0.49			GOA	−0.98
		Red+	0.16			Red+	−0.93
	RCP8.5	Red	0.43		RCP8.5	Red	−0.90
		GOA	−0.40			GOA	−0.99
GFDL-ESM2G		Red+	−1.22			Red+	−0.53
	RCP2.6	Red	−1.34		RCP2.6	Red	−0.49
		GOA	−0.90			GOA	−0.61
		Red+	−1.25			Red+	−0.59
	RCP4.5	Red	−1.36		RCP4.5	Red	−0.54
		GOA	−0.94			GOA	−0.68
		Red+	−1.21	GFDL model-ensemble mean		Red+	−0.66
	RCP6.0	Red	−1.30		RCP6.0	Red	−0.61
		GOA	−0.94			GOA	−0.75
		Red+	−1.32			Red+	−0.68
	RCP8.5	Red	−1.43		RCP8.5	Red	−0.64
		GOA	−1.00			GOA	−0.75

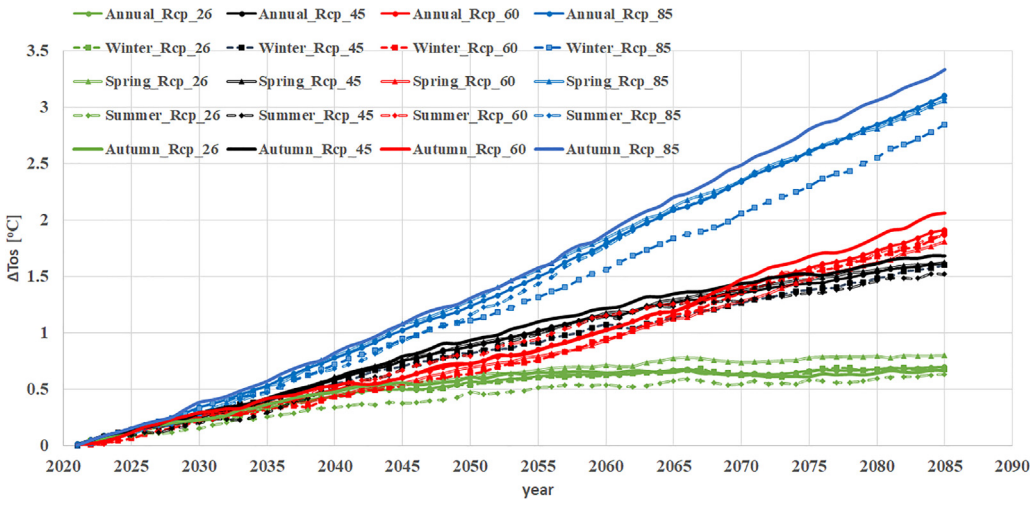

Figure 13 Thirty-year running annual means of projected sea surface temperatures (Tos) under the four representative concentration pathway scenarios studied (RCP2.6, RCP4.5, RCP6.0, and RCP8.5) relative to the 2006–2035 period for the GFDL-CM3 model simulation in Red+.

18 days (29/07/2012 to 15/08/2012) in the Gulf of Aqaba and for 14 days (14/07/2001 to 27/07/2001) in cluster 11.

Heatwave events have a negative effect on chlorophyll-*a* concentrations (as an indicator of bleaching) as described by Caputi et al. (2014). It is clear from Table 3 that the chl-a concentrations reached a minimum during heat wave events, indicating that the heat wave events have a negative effect on marine biota and may lead to thermal collapse, especially because the Red Sea is a semi-enclosed basin (marine biota cannot migrate north). This result is in accordance with the previous findings of Maor-Landaw et al. (2014) and Chaidez et al. (2017).

3.7. Projected sea surface temperature (Tos) scenario calculations

3.7.1. Model performance under the control period, 2006–2016

GFDL exhibits relatively good skills in modeling Tos in some regions including the eastern Bering Sea, Gulf of Alaska and Insular Pacific Islands–Hawaii (Hervieux et al., 2017; Stock et al., 2011). However, this model has shown relatively lower abilities in other regions (e.g., California Current System; Jacox et al., 2017). Thus, the current analysis assessed three GFDL simulations (GFDL-ESM2M, GFDL-ESM2G, and GFDL-CM3) against OISST prior to use in the analysis of the projected warming scenario in Red+.

Table 4 shows the performance of three GFDL simulations under the RCP2.6, RCP4.5, RCP6.0 and RCP8.5 scenarios for three studied subbasins (the Red Sea, Red+ and GOA). The GFDL model ensemble mean of simulation was calculated for each scenario. To determine whether the simulation results overestimate or underestimate SST, the result was subjected to a *t*-test with 95% significance.

GFDL-CM3 simulations overestimate SST by approximately 0.30, 0.25, 0.05 and 0.16°C in Red+ under the RCP2.6, RCP4.5, RCP6.0 and RCP8.5 scenarios, respectively (Table 4). The GFDL-ESM2M, GFDL-ESM2G and GFDL model ensemble mean simulations show underestimations of SST in Red+ by approximately 1.22, 0.72 and 0.53°C, respectively, under the RCP2.6 scenario.

In general, the GFDL-CM3 simulation results best describe SST during the control period in comparison to the other studied simulations. This finding indicates that the upgrade from the old GFDL simulations to the most recent simulation (GFDL-CM3) improves the result significantly.

3.7.2. Future sea surface temperature, 2006–2100

The GFDL-CM3 simulation of projected SST scenarios in the current century indicates significant warming during the 2006–2100 period in the study area, especially for the RCP8.5 scenario (Fig. 13). The expected warming up to 2100 (hereafter $\Delta Tos = Tos_{2100} - Tos_{2006}$) ranges from 2.8–3.2°C under the RCP8.5 scenario, 1.75–2.1°C under the RCP6.0 scenario, 1.5–1.7°C under the RCP4.5 scenario and 0.6–0.85°C under the RCP2.6 scenario.

There is no significant regional variation in projected warming trends under the GFDL-CM3 simulation (data are not shown). However, there is a significant seasonal variation in projected warming trends, reaching the minimum values during the winter seasons under the RCP2.6, RCP6.0 and RCP8.5 scenarios and during summer during RCP4.5. The maximum values of the seasonal warming trend occurred during the spring season for RCP2.6 and during the autumn season for the RCP4.5, RCP6.0 and RCP8.5 scenarios.

The current research related the uncertainty in projected Tos to only two sources: the seasonal variations and the scenario used. The uncertainty associated with the region was not significant, while the uncertainty related to the simulation used was negligible as the research used only the best simulation that described the current SST. Uncertainties in projected ΔTos were estimated to be 2.6°C, where the scenario used and the seasonal variations account for 2.45°C and 0.25°C, respectively. Hoegh-Guldberg et al. (2014) showed that the uncertainties in projected ΔTos according to the scenario used is 2.57°C. Both of current and previous findings confirm that the emission assumptions dominating the uncertainties of different sources.

4. Conclusions

Based on the daily OISST time series, the current research studied the current SST changes in Red+ from 1982 to 2016. Moreover, GFDL model simulations were used to analyze the uncertainty of Red+ warming trends.

The results showed that the gridded OISST data is a relevant tool to study the SST in Red+ due to excellent OISST agreement with in situ data. Moreover, the finer OISST resolution (0.25°) seemed fine enough to analyze local-scale features of Red+. Thus, the current findings constitute a basis for future research seeking to study coastal phenomena such as coastal upwelling occurrence and its influence on SST variability, which is explicitly an updated topic.

The annual mean (from 1982 to 2016) of gridded OISST in Red+ confirms the presence of a 7°C spatial variation ranging from 22.5°C over grids concentrated in the northern part of the Gulf of Suez to 29.5°C over grids concentrated in the eastern part of SRed. The gridded OISST data confirms that the daily Red+ SST seldom falls outside the range of 20°C to 33°C. Moreover, the coldest years were 1984 and 1992 in Red+ and the Red Sea, respectively; however, the hottest year was 2010 in both Red+ and the Red Sea, and that was due to the dramatic drop of NAOI during 2010. In addition, the Red Sea and Red+ confirm a significant spatially warming trend (from 1982 to 2016) of 0.029°C yr^{-1} and 0.025°C yr^{-1}, respectively, peaking over NRed. However, NRed exhibits a more intensive warming trend than GOA and SRed; the SST in NRed remains cooler than in GOA and SRed. Generally, the intensive Red+ warming trend compared to the average global warming trend (0.011°C yr^{-1}) leads to an accelerated increase in the Red+ temperature together with associated increases in seawater acidification and decreases in oxygen level. This combination will duplicate risks to marine ecosystems, biodiversity and fisheries.

The Red+ SST describes a complex SST pattern with significant regional dependence and seasonal fluctuation of Red+ SST and warming trends, which should be considered in the future analysis of Red+. For example, simple modeling of Red+ based on dividing the study area into several subbasins should consider the uniform SST distribution in Red+.

The current research shows that the studied atmospheric parameters (T_{2m}, SLP, TCC, τ_{ac}, τ_{al}, F_n, Fsw, AMOI, NAOI, and ISMI) and SST, in general, are significantly correlated in most of the studied area. There is seasonal variation in the correlation coefficient between nine of the ten studied parameters and SST; however, ISMI shows no significant seasonal variation in the correlation coefficient with SST. Moreover, the influences of the thirteen studied atmospheric parameters on SST suggests that 98% of the daily Red+ SST variation can be explained by only T_{2m}, ISMI, SLP, τ_{ac}, and F_h before removing the annual cycle, while 77% can be explained after removal. In addition, the PCA results showed that the first five principal components can explain 90% of the overall variance before removing the annual cycle, while the first eight principal components can explain 90% of the

overall variance after removing the annual cycle, highlighting the importance of the annual cycle in the correlation between the studied parameters.

As expected, the chl-a concentration during the heat wave events decreased by approximately 33% from its annual average values. In the warm environment of the Red Sea, the temperature is expected to increase in the future (according to the GFDL-CM3 projection results), which would lead to more frequently occurring future heat events. Thus, Red Sea marine organisms are clearly extremely vulnerable to heat wave events, especially because the Red Sea is a semi-enclosed basin, and marine organisms cannot migrate north. This finding highlights the need to develop reasonable mitigation/adaptation tools to cope with the future warming issues during the current century, including the issue of chl-a growth vulnerability.

To support future management in Red+, Tos up to 2100 were described by GFDL-CM3 that best describe the recent Red+ SST. The GFDL-CM3 simulations showed that ΔTos ranges from 3.2°C during autumn under the RCP8.5 scenario to 0.6°C during summer under the RCP2.6 scenario, where the emissions used and seasonal variations account for 90% and 10%, respectively, of the studied uncertainty. This finding indicates that more global management efforts are needed to reduce green gas emissions.

The current results provide a context for descriptive and statistical analyses describing recent and future SST over Red+ in terms of annual and seasonal cycles. In comparison to the previous scientific studies in the region, the current study improves our understanding of SST and the associated phenomena for the period 1982–2100. The current paper gives the first scientific comparison between different studied subbasins to understand spatial SST variations. Moreover, the current paper classifies the Red+ into 16 clusters to match heat wave occurrence with chl-a concentration for each cluster to qualify the thermal effect on marine biota. Moreover, the current research analyses the SST projection over Red+ up to 2100 to understand future warming uncertainty. This result provides a powerful scientific tool to coop with climate change.

Acknowledgements

The author would like to thank Mr. Mohamed Gad at the National Institute of Oceanography and Fisheries, Egypt, for his valuable comments. This research work is part of a research project sponsored by: IDRC-Canada for establishing Alexandria Research Centre for Adaptation to Climate Change (ARCA), Alexandria University, Egypt.

Appendix A. Supplementary data

Supplementary data associated with this article can be found, in the online version, at https://doi.org/10.1016/j.oceano.2019.05.002.

References

Adcroft, A., Hallberg, R., 2006. On methods for solving the oceanic equations of motion in generalized vertical coordinates. Ocean Model. 11, 224–233.

Aiki, H.A., Takahashi, K., Yamagata, T., 2006. The Red Sea outflow regulated by the Indian Monsoon. Cont. Shelf Res. 26, 1448–1468.

Al-Horani, F.A., Al-Rousan, S.A., Al-Zibdeh, M., Khalaf, M.A., 2006. The status of coral reefs on the Jordanian coast of the Gulf of Aqaba, Red Sea. Zool. Middle East 38, 99–110, http://dx.doi.org/10.1080/09397140.2006.10638171.

Anderson, J.L., Balaji, V., Broccoli, A.J., Cooke, W.F., Delworth, T.L., Dixon, K.W., Donner, L.J., Dunne, K.A., Freidenreich, S.M., 2004. The new GFDL global atmosphere and land model AM2-LM2: evaluation with prescribed SST simulations. J. Climatol. 17, 4641–4673, http://dx.doi.org/10.1175/JCLI-3223.1.

Anonymous, 2014. NASA Goddard Space Flight Center, Ocean Ecology Laboratory, Ocean Biology Processing Group: Sea-viewing Wide Field-of-view Sensor (SeaWiFS) Ocean Color Data, NASA OB.DAAC, accessed on 2016/02/29, 10.5067/ORBVIEW-2/SEAWIFS_OC.2014.0.

Bai, Y., He, X., Yu, S., Chen, C., 2018. Changes in the ecological environment of the marginal seas along the Eurasian continent from 2003 to 2014. Sustainability 10, article no. 635, 15 pp., http://dx.doi.org/10.3390/su10030635.

Banzon, V., Reynolds, R., Coauthors, 2018. The Climate Data Guide: SST data: NOAA Optimal Interpolation (OI) SST Analysis, version 2 (OISSTv2) 1x1, accessed 17 December 2018, https://climatedataguide.ucar.edu/climate-data/sst-data-noaa-optimal-interpolation-oi-sst-analysis-version-2-oisstv2-1x1.

Belkin, I., Rapid, M., 2009. Warming of large marine ecosystems. Prog. Oceanogr. 81, 207–213.

Bentamy, A., Croize-Fillon, D., 2012. Gridded surface wind fields from Metop/ASCAT measurements. Int. J. Remote Sens. 33 (6), 1729–1754, http://dx.doi.org/10.1080/01431161.2011.600348.

Berman, T., Paldor, N., Brenner, S., 2003. Annual SST cycle in the Eastern Mediterranean, Red Sea and Gulf of Elat. Geophys. Res. Lett. 30, 1261, http://dx.doi.org/10.1029/2002GL015860.

Bower, A.S., Furey, H.H., 2012. Mesoscale eddies in the Gulf of Aden and their impact on the spreading of Red Sea Outflow Water. Prog. Oceanogr. 96, 14–39.

Boyer, T.P., Antonov, J.I., Baranova, O.K., Coleman, C., Garcia, H.E., Grodsky, A., Johnson, D.R., Locarnini, R.A., Mishonov, A.V., O'Brien, T.D., Paver, C.R., Reagan, J.R., Seidov, D., Smolyar, I. V., Zweng, M.M., 2013. World Ocean Database 2013. NOAA Atlas NESDIS, 72. NOAA Printing Office, Silver Spring, MD, 208 pp., http://hdl.handle.net/11329/357.

Brewin, R.J.W., Raitsos, D.E., Pradhan, Y., Hoteit, I., 2013. Comparison of chlorophyll in the Red Sea derived from MODIS-Aqua and in vivo fluorescence. Remote Sens. Environ. 136, 218–224, http://dx.doi.org/10.1016/j.rse.2013.04.018.

Cantin, N.E., Cohen, A.L., Karnauskas, K.B., Tarrant, A.M., McCorkle, D.C., 2010. Ocean warming slows coral growth in the central Red Sea. Science 329 (5989), 322–325.

Caputi, N., Jackson, G., Pearce, A.F., 2014. The marine heat wave off Western Australia during the summer of 2010/11 – 2 years on. Fisheries Res. Rep. No. 250. Dpt. Fisheries, Western Australia, 40 pp.

Chaidez, V., Dreano, D., Agusti, S., Duarte, C.M., Hoteit, I., 2017. Decadal trends in Red Sea maximum surface temperature. Sci. Rep. 7, article no. 8144, http://dx.doi.org/10.1038/s41598-017-08146-z.

Collins, M., Knutti, R., Arblaster, J., Dufresne, J.L., Fichefet, T., Friedlingstein, P., Gao, X., Gutowski, W.J., Johns, T., Krinner, G., Shongwe, M., Tebaldi, C., Weaver, A.J., Wehner, M., 2013. Long-term climate change: projections, commitments and irreversibility. In: Stocker, T.F., Qin, D., Plattner, G.-K., Tignor, M., Allen, S. K., Boschung, J., Nauels, A., Xia, Y., Bex, V., Midgley, P.M. (Eds.), Climate Change 2013: The Physical Science Basis. Contribution of Working Group I to the Fifth Assessment Report of the Intergovernmental Panel on Climate Change. Cambridge University Press, Cambridge, 1535 pp.

Dee, D.P., Uppala, S.M., Simmons, A.J., Berrisford, P., Poli, P., Kobayashi, S., Andrae, U., Balmaseda, M.A., Balsamo, G., Bauer, D.P., 2011. The ERA-Interim reanalysis: configuration and performance of the data assimilation system. Q. J. R. Meteorolog. Soc. 137, 553–597, http://dx.doi.org/10.1002/qj.828.

Delworth, T.L., Broccoli, A.J., Rosati, A., Stouffer, R.J., Balaji, V., Beesley, J.A., Cooke, W.F., Dixon, K.W., Dunne, J., Dunne, K.A., Durachta, J.W., Findell, K.L., Ginoux, P., Gnanadesikan, A., Gordon, C.T., Griffies, S.M., Gudgel, R., Harrison, M.J., Held, I.M., Hemler, R.S., Horowitz, L.W., Klein, S.A., Knutson, T.R., Kushner, P.J., Langenhorst, A.R., Lee, H., Lin, S., Lu, J., Malyshev, S.L., Milly, P.C., Ramaswamy, V., Russell, J., Schwarzkopf, M.D., Shevliakova, E., Sirutis, J.J., Spelman, M.J., Stern, W.F., Winton, M., Wittenberg, A.T., Wyman, B., Zeng, F., Zhang, R., 2006. GFDL's CM2 Global Coupled Climate Models. Part I: Formulation and simulation characteristics. J. Climatol. 19, 643–674, http://dx.doi.org/10.1175/JCLI3629.1.

Donner, L.J., Wyman, B.L., Hemler, R.S., Horowitz, L.W., Ming, Y., Zhao, M., Golaz, J., Ginoux, P., Lin, S., Schwarzkopf, M.D., Austin, J., Alaka, G., Cooke, W.F., Delworth, T.L., Freidenreich, S.M., Gordon, C.T., Griffies, S.M., Held, I.M., Hurlin, W.J., Klein, S.A., Knutson, T.R., Langenhorst, A.R., Lee, H., Lin, Y., Magi, B.I., Malyshev, S.L., Milly, P.C., Naik, V., Nath, M.J., Pincus, R., Ploshay, J.J., Ramaswamy, V., Seman, C.J., Shevliakova, E., Sirutis, J.J., Stern, W.F., Stouffer, R.J., Wilson, R.J., Winton, M., Wittenberg, A.T., Zeng, F., 2011. The dynamical core, physical parameterizations, and basic simulation characteristics of the atmospheric component AM3 of the GFDL Global Coupled Model CM3. J. Climatol. 24, 3484–3519, http://dx.doi.org/10.1175/2011JCLI3955.1.

Dunne, P.J., John, G.J., Shevliakova, E., Stouffer, J.R., Krasting, P.J., Malyshev, L.S., Milly, D.C.P., Sentman, T.L., Adcroft, J.A., Cooke, W., Dunne, A.K., Stephen, M., Griffies, M.S., Hallberg, W.R., Harrison, J.M., Levy, H., Wittenberg, T.A., Peter, J., Phillips, J. P., Zadeh, N., 2013. GFDL's ESM2 global coupled climate–carbon earth system models. Part II: Carbon system formulation and baseline simulation characteristics. J. Climatol. 26, 2247–2267, http://dx.doi.org/10.1175/JCLI-D-12-00150.1.

Eladawy, A., Nadaoka, K., Negm, A., Abdel-Fattah, S., Hanafy, A., Shaltout, M., 2017. Characterization of the northern Red Sea's oceanic features with remote sensing data and outputs from a global circulation model. Oceanologia 59 (3), 213–237, http://dx.doi.org/10.1016/j.oceano.2017.01.002.

GOSUD, 2016. GOSUD Project-Global Ocean Surface Underway data. SEANOE (SEA scieNtific Open data Edition), http://dx.doi.org/10.17882/47403.

Griffies, S.M., 2009. Elements of MOM4p1. GFDL Ocean Group Tech. Rep. No. 6, 444 pp., https://www.gfdl.noaa.gov/wp-content/uploads/files/model_development/ocean/guide4p1.pdf.

Griffies, S.M., Winton, M., Donner, L.J., Horowitz, L.W., Downes, S. M., Farneti, R., Gnanadesikan, A., Hurlin, W.J., Lee, H., Liang, Z., Palter, J.B., Samuels, B.L., Wittenberg, A.T., Wyman, B.L., Yin, J., Zadeh, N., 2011. The GFDL CM3 Coupled Climate Model: Characteristics of the ocean and sea ice simulations. J. Climatol. 24, 3520–3544, http://dx.doi.org/10.1175/2011JCLI3964.1.

Halliwell, G.R., 2004. Evaluation of vertical coordinate and vertical mixing algorithms in the HYbrid-Coordinate Ocean Model (HYCOM). Ocean Model. 7 (3), 285–322, http://dx.doi.org/10.1016/j.ocemod.2003.10.002.

He, Z., Wu, R., Wang, W., Wen, Z., Wang, D., 2017. Contributions of surface heat fluxes and oceanic processes to tropical SST changes: seasonal and regional dependence. J. Climatol. 30, 4185–4205, http://dx.doi.org/10.1175/JCLI-D-16-0500.1.

Hervieux, G., Alexander, M.A., Stock, C.A., Jacox, M.G., Pegion, K., Becker, E., Castruccio, F., Tommasi, D., 2017. More reliable coastal SST forecasts from the North American multimodel ensemble. Clim. Dyn., http://dx.doi.org/10.1007/s00382-017-3652-7.

Hoegh-Guldberg, O., Cai, R., Poloczanska, E.S., Brewer, P.G., Sundby, S., Hilmi, K., Fabry, V.J., Jung, S., 2014. The ocean – supplementary material. In: Barros, V.R., Field, C.B., Dokken, D. J., Mastrandrea, M.D., Mach, K.J., Bilir, T.E., Chatterjee, M., Ebi, K.L., Estrada, Y.O., Genova, R.C., Girma, B., Kissel, E.S., Levy, A. N., MacCracken, S., Mastrandrea, P.R., White, L.L. (Eds.), Climate Change 2014: Impacts, Adaptation, and Vulnerability. Part B: Regional Aspects. Contribution of Working Group II to the Fifth Assessment Report of the Intergovernmental Panel on Climate Change. Cambridge University Press, Cambridge, 1655–1731, accessed on 29 April 2019, https://www.ipcc.ch/site/assets/uploads/2018/02/WGIIAR5-Chap30_FINAL.pdf.

Hurrell, J.W., 1995. Decadal trends in the North Atlantic Oscillation regional temperatures and precipitation. Science 269, 676–679.

IPCC, 2014. Climate Change 2013 – The Physical Science Basis: Working Group I Contribution to the Fifth Assessment Report of the Intergovernmental Panel on Climate Change. Cambridge University Press, Cambridge, 1535 pp., http://dx.doi.org/10.1017/CBO9781107415324.

Jacox, M.G., Alexander, M.A., Stock, C.A., Hervieux, G., 2017. On the skill of seasonal sea surface temperature forecasts in the California Current System and its connection to ENSO variability. Clim. Dyn., http://dx.doi.org/10.1007/s00382-017-3608-y.

Jolliffe, I.T., 2002. Principal Component Analysis, 2nd edn. Springer, New York, 518 pp.

Karnauskas, K.B., Jones, B.H., 2018. The interannual variability of sea surface temperature in the Red Sea from 35 years of satellite and in situ observations. J. Geophys. Res. 123, 5824–5841, http://dx.doi.org/10.1029/2017JC013320.

Large, W.G., Pond, S., 1981. Open ocean momentum flux measurements in moderate to strong winds. J. Phys. Oceanogr. 11, 324–336, http://dx.doi.org/10.1175/1520-0485(1981)011<0324:OOMFMI>2.0.CO;2.

MacQueen, J.B., 1967. Some methods for classification and analysis of multivariate observations. In: Proc. 5th Berkeley Symposium on Mathematical Statistics and Probability. University of California Press, Berkeley, 281–297.

Maor-Landaw, K., Karako-Lampert, S., Waldman Ben-Asher, H., Goffredo, S., Falini, G., Dubinsky, Z., Levy, O., 2014. Gene expression profiles during short-term heat stress in the red sea coral *Stylophora pistillata*. Global Change Biol. 20 (10), 3026–3035.

Milly, P.C., Malyshev, S.L., Shevliakova, E., Dunne, K.A., Findell, K.L., Gleeson, T., Liang, Z., Phillipps, P., Stouffer, R.J., Swenson, S., 2014. An enhanced model of land water and energy for global hydrologic and earth-system studies. J. Hydrometeorol. 15, 1739–1761, http://dx.doi.org/10.1175/JHM-D-13-0162.1.

Nykjaer, L., 2009. Mediterranean Sea surface warming 1985–2006. Clim. Res. 39, 11–17, http://dx.doi.org/10.3354/cr00794.

Osman, E.O., Smith, D.J., Ziegler, M., Kürten, B., Conrad, C., El-Haddad, K.M., Voolstra, C.R., Suggett, D.J., 2018. Thermal refugia against coral bleaching throughout the northern Red Sea. Global Change Biol. 24, e474–e484.

Owens, R.G., Hewson, T.D., 2018. European Centre for Medium-Range Weather Forecasts Forecast User Guide. ECMWF, Reading, http://dx.doi.org/10.21957/m1cs7h.

Qu, B., Gabric, A., Zhu, J., Lin, D., Qian, F., Zhao, M., 2012. Correlation between sea surface temperature and wind speed in Greenland Sea and their relationships with NAO variability. Water Sci. Eng. 5 (3), 304–315, http://dx.doi.org/10.3882/j.issn.1674-2370.2012.03.006.

Raitsos, D.E., Hoteit, I., Prihartato, P.K., Chronis, T., Triantafyllou, G., Abualnaja, Y., 2011. Abrupt warming of the Red Sea. Geophys. Res. Lett. 38, article no. L14601, http://dx.doi.org/10.1029/2011GL047984.

Reynolds, R.W., 2009. What's New in Version 2 of daily optimum interpolation (OI) sea surface temperature (SST) analysis, 10 pp., https://www.ncdc.noaa.gov/sites/default/files/attachments/Reynolds2009_oisst_daily_v02r00_version2-features.pdf.

Reynolds, R.W., Smith, T.M., Liu, C., Chelton, D.B., Casey, K.S., Schlax, M.G., 2007. Daily high-resolution blended analyses for sea surface temperature. J. Climatol. 20, 5473–5496, http://dx.doi.org/10.1175/2007JCLI1824.1.

Ricciardulli, L., Wentz, F.J., Smith, D.K., 2011. Remote Sensing Systems QuikSCAT Ku-2011 Daily Orbital Swath Ocean Vector Winds L2B, Version 4. Remote Sensing Systems, Santa Rosa. CA. Available online at www.remss.com/missions/qscat. [Accessed 01/04/2019].

Richardson, A.J., Schoeman, D.S., 2004. Climate impact on plankton ecosystems in the northeast Atlantic. Science 305, 1609–1612, http://dx.doi.org/10.1126/science.1100958.

Roik, A., Roder, C., Rothig, T., Voolstra, C.R., 2016. Spatial and seasonal reef calcification in corals and calcareous crusts in the central Red Sea. Coral Reefs 35, 681–693.

Samelson, R.M., Skyllingstad, E.D., Chelton, D.B., Esbensen, S.K., O'Neill, L.W., Thum, N., 2006. On the coupling of wind stress and sea surface temperature. J. Climatol. 19 (8), 1557–1566, http://dx.doi.org/10.1175/JCLI3682.1.

Sarthia, P.P., Dash, S.K., Mamgain, A., 2012. Possible changes in the characteristics of Indian Summer Monsoon under warmer climate. Global Planet. Change 92, 17–29, http://dx.doi.org/10.1016/j.gloplacha.2012.03.006.

Sawall, Y., Al-Sofyani, A., Banguera-Hinestroza, E., Voolstra, C.R., 2014. Spatio-temporal analyses of *Symbiodinium* physiology of the coral *Pocillopora verrucosa* along large-scale nutrient and temperature gradients in the Red Sea. PLoS ONE 9 (8), article no. e103179, http://dx.doi.org/10.1371/journal.pone.0103179.

Shaltout, M., Omstedt, A., 2014. Recent sea surface temperature trends and future scenarios for the Mediterranean Sea. Oceanologia 56 (3), 411–443, http://dx.doi.org/10.5697/oc.56-3.411.

Skliris, N., Sofianos, S., Gkanasos, A., Mantziafou, A., Vervatis, V., Axaopoulos, P., Lascaratos, A., 2012. Decadal scale variability of sea surface temperature in the Mediterranean Sea in relation to atmospheric variability. Ocean Dyn. 62, 13–30, http://dx.doi.org/10.1007/s10236-011-0493-5.

Smeed, D., 1997. Seasonal variation of the flow in the strait of Bab al Mandab. Oceanol. Acta 20 (6), 773–781.

Stock, C.A., Alexander, M.A., Bond, N.A., Brander, K.M., Cheung, W.W., Curchitser, E.N., Delworth, T.L., Dunne, J.P., Griffies, S.M., Haltuch, M.A., 2011. On the use of IPCC-class models to assess the impact of climate on living marine resources. Prog. Oceanogr. 88, 1–27.

Thomas, M.K., Kremer, C.T., Klausmeier, C.A., Litchman, E., 2012. A global pattern of thermal adaptation in marine phytoplankton. Science 338, 1085–1088.

Trenberth, K.E., Large, W.G., Olson, J.G., 1990. The mean annual cycle in global ocean wind stress. J. Phys. Oceanogr. 20 (11), 1742–1760, http://dx.doi.org/10.1175/1520-0485(1990)020<1742:TMACIG>2.0.CO;2.

Trenberth, K.E., Shea, D.J., 2006. Atlantic hurricanes and natural variability in 2005. Geophys. Res. Lett. 33, article no. L12704, http://dx.doi.org/10.1029/2006GL026894.

Wang, B., Wu, R., Lau, K., 2001. Interannual variability of Asian summer monsoon: contrast between the Indian and western North Pacific-East Asian monsoons. J. Climatol. 14, 4073–4090.

Wang, C., Weisberg, R.H., Yang, H., 1999. Effects of the wind speed-evaporation-SST feedback on the El Niño-Southern Oscillation. J. Atmos. Sci. 56 (10), 1391–1403, http://dx.doi.org/10.1175/1520-0469(1999)0562.0.CO;2.

Wilson, S., Rebecca, K., 2000. The Gulf of Aden. In: Sheppard, C. (Ed.), Seas at the Millennium: An Environmental Evaluation. Elsevier Science, Oxford, 47–61.

Worley, S.J., Woodruff, S.D., Reynolds, R.W., Lubker, S.J., Lott, N., 2005. ICOADS release 2.1 data and products. Int. J. Climatol. 25, 823–842.

You, Q., Jiang, Z., Moore, G.W.K., Bao, Y., Kong, L., Kang, S., 2017. Revisiting the relationship between observed warming and surface pressure in the Tibetan Plateau. J. Climatol. 30, 1721–1737, http://dx.doi.org/10.1175/JCLI-D-15-0834.1.

Zhou, C., Wang, K., 2016. Evaluation of surface fluxes in ERA-Interim using flux tower data. J. Climatol. 29, 1573–1582, http://dx.doi.org/10.1175/JCLI-D-15-0523.1.